Night light polarization: modeling and observations of light pollution in the presence of aerosols and background skylight or airglow

Léo Bosse[1], Jean Lilensten[1,5], Nicolas Gillet[2], Colette Brogniez[3], Olivier Pujol[3], Sylvain Rochat[1], Alain Delboulbé [1], Stéphane Curaba[1], Magnar G. Johnsen[4]

[1]Institut de Planétologie et d'Astrophysique de Grenoble (IPAG) CNRS – UGA, France
[2]Univ. Grenoble Alpes, Univ. Savoie Mont Blanc, CNRS, IRD, UGE, ISTerre, 38000 Grenoble, France
[3]Univ. Lille, CNRS, UMR 8518 – LOA – Laboratoire d'Optique Atmosphérique, F-59000 Lille, France
[4]Tromsø Geophysical Observatory, UiT - the Arctic University of Norway, Tromsø, Norway
[5]Honorary astronomer at Royal Observatory of Belgium, Brussels

Key Points:

- First polarized radiative transfer code for night light and atmospheric studies including Lorenz-Mie and Rayleigh polarized scattering.
- Application to aerosols, light pollution and thermospheric nightglow studies.
- Validation through specific measurements at different wavelengths

Corresponding author: Léo Bosse, leo.bosse@univ-grenoble-alpes.fr

Abstract

Aurorae and nightglow are faint atmospheric emissions visible during night-time at several wavelengths. These emissions have been extensively studied but their polarization remains controversial. A great challenge is that light pollution from cities and scattering in the lower atmosphere interfere with polarization measurements. We introduce a new polarized radiative transfer model able to compute the polarization measured by a virtual instrument in a given nocturnal environment recreating real world conditions (atmospheric and aerosol profiles, light sources with complex geometries, terrain obstructions). The model, based on single scattering equations in the atmosphere, is tested on a few simple configurations to assess the effect of several key parameters in controlled environments. Our model constitutes a proof of concept for polarization measurements in nocturnal conditions, that calls for further investigations. In particular, we discuss how multiple-scattering (neglected in the present study) could impact our observations and their interpretation, and the future need for inter-calibrating the source and the polarimeter in order to optimally extract the information contained in this kind of measurements. The model outputs are compared to field measurements in five wavelengths. A convincing fit between the model predictions and observations is found in the three most constrained wavelengths despite the single scattering approximation. Several applications of our model are discussed that concern the polarization of aurorae, the impact of light pollution, or aerosols and air pollution measurements.

Plain Language Summary

The darkest night is not black. It is actually quite luminous: The upper atmosphere emits its own glow, called *nightglow*; there is also the light from the stars, that from artificial sources, and their possible reflections, on snow for example. All these lights are further scattered in the atmosphere by the air molecules and/or the aerosols (dust, ice crystals, droplets...). This scattering makes the light waves oscillate in a privileged direction: it becomes *polarized*. In this article, we use a dedicated instrument that we developed (a polarimeter), along with a numerical code called POMEROL that accounts for all the above sources. We show that polarization may be used for studying the nightglow, light pollution or aerosols, with several possible applications in ecology, atmospheric sciences and space weather.

1 Introduction

The main auroral emissions are due to the atomic oxygen and molecular ion nitrogen N_2^+. The former produces the red (630 nm) and green (557.7 nm) light at the altitudes of about 220 and 110 km respectively. The latter emits in a large band amongst which the most prominent emissions are the blue (427.8 nm) and the purple (391.4 nm) radiation, around an altitude of 85 km. They mainly originate in the collisions between precipitated electrons and the ambient atmosphere (see for example Banks & Kockarts, 1973).

These emissions are pronounced at high latitudes, in the auroral ovals. At other latitudes, emissions of the upper atmosphere are called *nightglow* (Leinert et al., 1998). The literature is abundant and here we only refer to some recent works. Emissions exist at all latitudes (Parihar et al., 2018). Their origin is due to chemical reactions (Plane et al., 2012) and collisions, either between neutral molecules or atoms, or between ambient ionospheric electrons and gases (Tashchilin & Leonovich, 2016). The drivers may be gravity waves (Vargas, 2019) or ionospheric currents (Dymond et al., 2019).

For the last decade, a serie of experiments have shown that the red emission, when measured from the ground, is polarized (Lilensten et al., 2016, and references herein). The direction of polarization for this red line was shown theoretically to be parallel to the magnetic field (Bommier et al., 2011). Correlations between variations in the magnetic field and in the angle of linear polarization (*AoLP*) had indeed been observed experimentally, but not systematically, with a first prototype of auroral polarimeter (Lilensten et al., 2008).

Recently, a new nightglow polarimeter has been developed in order to observe faint emissions (i.e. not limited to bright aurorae). It also allows to target simultaneously several atmospheric emissions (for a full description, see Bosse et al., 2020). Three findings by Bosse et al. (2020) lead us to reconsider our first understanding of the upper atmosphere polarization:

- All of the four auroral emission lines appear polarized when measured from the ground,
- Although in several circumstances this polarization appears to be linked to the local magnetic activity and to the state of the ionosphere, it is far from being systematically aligned on the apparent direction of the magnetic field, as foreseen theoretically,
- Light pollution from nearby cities significantly impacts, via scattering, the polarization measurements.

These series of observations questioned the geophysical origin of the polarization: how much is it affected by light pollution scattering in the lower atmosphere? Are auroral lights polarized at the emission or during their propagation toward to the instrument? To answer these questions, it is necessary to develop a polarized radiative transfer code able to account for sources potentially spread all over both the sky and the ground.

In this paper, we describe the first code developed to this purpose, called 'POMEROL' (standing for 'POlarisation par Mie Et Rayleigh des Objets Lumineux' which translates to 'Luminous Objects Polarization by Mie and Rayleigh Scattering'). It takes into account the light emitted in the upper atmosphere, as well as all possible pollution sources on the ground. We present some examples of applications, with comparisons to geophysical data obtained in the French Alps. In this paper the code is restricted to a single scattering approximation (SSA). The goal here is to prove the feasibility of night-time polarization measurements. Thus, the model is currently kept as simple as possible. We show that even in this relatively simple configuration, it is possible to reproduce quite well the measurements and to deduce physical parameters behind the polarization. However, we also discuss the limitations of this first approach, and what improvements could be brought by considering a polarized multiple scattering radiative scheme. In this first paper about night-time polarization, we think it is useful to know what the single scattering approximation can give before diving into the complexity of multiple scattering. We will see that the SSA can already catch the essence of the physics at hand. Our study paves the way to future investigations of the night-light polarization, and calls for evolution of the model, including in particular multiple scattering.

Such a code is not designed only to better understand the upper atmosphere. It could also help to characterize aerosols in a passive experimental way in the absence of the moon or the sun. It may also lead to more accurate monitoring of light pollution, which represents a growing concern over the last decades. The area covered by light from human origin is spreading, along with its impacts on life (Grubisic et al., 2018), energy consumption (Kyba et al., 2017) or astronomy. Among the literature displaying a varied list of negative effects, we can cite the insect population decline and the "Ecological Armageddon" (Grubisic et al., 2018) or health issues (Garcia-Saenz et al., 2018; Zielinska-Dabkowska, 2018). Most of the studies concentrates on the exposure rate and magnitude. However, we lack studies on light pollution polarization (Horvath et al., 2009; Kyba et al., 2011). Yet it plays an important role for vast groups of insects that use it to navigate.

Below, we briefly describe the instrument in Section 2. We then present the principles of the radiative transfer model in Section 3.2 (the full details are given in Appendix A). Next we provide in Section 4 a series of synthetic experiments in order to assess the influence of the input parameters: effect of a localized source on the ground, of atmospheric properties (ozone, aerosols) and of multiple scattering. In Section 5, we compare the measurements from an experimental campaign at mid-latitude to the model outputs. Finally, we discuss our findings in Section 6.

2 Description of the polarimeter

Here is a brief overview of the experimental set-up. The polarimeter used in this study has been fully described in Bosse et al. (2020). We therefore only recall here its basics.

The incoming light along the line of sight is filtered through a narrow optical filter (of 2 nm width for the red line and 10 nm width for all other lines). Behind it a polarizing lens rotates at 2 Hz. The light passing the lens then hits a photomultiplier and is converted into an electrical current with a 1 kHz sampling rate. Data are smoothed over a given time window during which the polarization is assumed constant (10 seconds for all data presented here). A lock-in analysis is performed in real time. This powerful method allows a fast and accurate computation of the polarization. However, when the degree of linear polarization (*DoLP*) becomes too small, typically below 0.5%, the *AoLP* can hardly be computed and becomes very noisy. Both the *DoLP* and *AoLP* have been calibrated, but not the radiant flux.

We note F_0 the incident radiant flux received at a given wavelength (note that all units given in this paper follow the National Institute of Standards and Technology (NIST)). The *DoLP* ranges between 0 and 1 (or, in the figures, 0 to 100%), and we define the *AoLP* with respect to the vertical (0° being upward, $\pm 90^\circ$ horizontal as it is π-periodic). φ_t is the angle of the polarizing filter with the vertical at time t. We suppose F_0, *DoLP* and *AoLP* to not change during one rotation of the polarizing filter. From basic optics, the radiant flux passing through the polarizing filter can be decomposed in two parts: a polarized one that varies as $\cos^2(\varphi_t - AoLP)$, and an unpolarized part, assumed to be constant over one rotation. For an incident radiant flux F_0, the polarized and unpolarized fluxes are

$$\left\{ \begin{array}{rcl} F_0^{pola} & = & DoLP \times F_0 \\ F_0^{unpola} & = & (1 - DoLP) \times F_0 \end{array} \right. . \tag{1}$$

Following Malus Law, after the polarizing filter they become

$$\left\{ \begin{array}{rcl} F_t^{pola} & = & F_0^{pola} \cos^2(\varphi_t - AoLP) \\ F_t^{unpola} & = & F_0^{unpola}/2 \end{array} \right. . \tag{2}$$

The $1/2$ factor on the unpolarized radiant flux comes from the averaging of Malus law over all *AoLP*. The radiant flux measured at time t can therefore be written as:

$$F_t = F_t^{pola} + F_t^{unpola} = F_0 \left(DoLP \times \cos^2(\varphi_t - AoLP) + \frac{1 - DoLP}{2} \right) . \tag{3}$$

Over one rotation of period T_r, this allows computing the Stokes parameters in spherical coordinates as:

$$\left\{ \begin{array}{rcl} I & = & \dfrac{1}{T_r} \displaystyle\int_0^{T_r} F_t dt \\ Q & = & \dfrac{1}{T_r} \displaystyle\int_0^{T_r} F_t \cos 2\varphi_t dt \\ U & = & -\dfrac{1}{T_r} \displaystyle\int_0^{T_r} F_t \sin 2\varphi_t dt \end{array} \right. . \tag{4}$$

Note that we do not consider circularly polarized light, such that the last Stokes parameter $V = 0$. The unit of the Stokes parameters as given here are nW, as it is the unit of the radiant flux measured by the instrument. To convert to nW/m^2/sr, we can simply divide them by the following coefficient depending on the instrument captor surface area Σ and half-opening angle ϵ: $2\pi\Sigma(1 - \cos(\epsilon))$. Injecting (3) in (4), one deduces the polarization parameters:

$$\left\{ \begin{array}{rcl} F_0 & = & 2I \\ DoLP & = & \dfrac{2}{I} \sqrt{Q^2 + U^2} \\ AoLP & = & \dfrac{1}{2} \arctan\left(\dfrac{U}{Q} \right) \end{array} \right. \tag{5}$$

The data may be smoothed over time by averaging I, Q and U over the desired number of rotations and then calculating the corresponding polarization values.

3 The radiative transfer model

In order to interpret the data from the instrument described in Section 2, we need to solve the polarized radiative transfer equations. This is the goal of the POMEROL code. We describe its inputs in Section 3.1 while the polarized radiative transfer equations are summarized in Section 3.2 and fully described in Appendix A. For the purpose of the present study, our analysis is based on single scattering. The limits of this approximation are discussed later on in Section 4.4. We aim at modeling the polarization observations under different configurations. We thus consider potentially several sources of light: direct light (from the nightglow, or the star-light), single scattered light (e.g. from cities, or auroral lights at high latitude).

3.1 Inputs of the model

3.1.1 Instrument related entries

The experimental characteristics are the first inputs, in particular the surface $\Sigma = 20$ cm^2 of the detector and its half aperture angle $\varepsilon = 1^\circ$, as well as its geographical position (latitude, longitude and altitude) and its pointing direction. This latter is defined by the elevation e (angle between the horizontal and the line of sight) and the azimuth a, reckoned with respect to the North, positive Eastward, i.e. clockwise rotation. One can specify discrete azimuths and elevations, or span over an *almucantar* (i.e. a full rotations in azimuth at a constant elevation) automatically.

3.1.2 Cities and pollution map

The model also takes as input a light pollution map. These are ground images of Earth at night produced by the NOAA Earth Observations Group, using satellite data from the Visible Infrared Imaging Radiometer Suite Day/Night Band. These images sum the emissions for wavelengths from 500 to 900 nm (Elvidge et al., 2013; Mills et al., 2013; Miller et al., 2013). The ground emissions are in units of nW/m^2/sr. The maps are processed by their authors to remove ephemeral light and are averaged over one year. They are provided by their authors in two modes, with the minimum emission set to zero or not. At high latitudes, auroral light are not always removed with other ephemeral lights, thus emission maps are overestimated. To better suppress the auroral contribution to the ground emission map, we use the second mode. At mid-latitude, the difference is minimal and we use the same mode for consistency. We use the most recent release from 2016. As the emission spectra of light pollution varies with location and time, we are unable to retrieve the radiance at each wavelength of interest. Thus, in the following, radiance unit is given in nW/m^2/sr and a linear inter-calibration of the model output and the observational data units is needed.

The map is centered on the instrument in polar coordinates (see Figure 9). The maximum range from the instrument (typically up to 200 km) and the number of bins (the best resolution being that of the map, namely 46 m) are adjustable parameters. To reduce artifacts due to digitization, the size of the bins increases with the square root of the distance to the instrument.

We can also consider instead synthetic emission maps. For example, these may consist of a point source of given radiance at a given distance, azimuth and elevation with respect to the instrument, or a uniform emission map of given radiance.

3.1.3 Natural background

In the following, the *natural background* light designates any source of light from the sky that we approximate as constant and isotropic. It includes two main contributions: the nightglow (Leinert et al., 1998) and the integrated starlight (e.g. Staude, 1975). The nightglow is specific as it is well defined in wavelengths (see Table 3). Its emissions can change with time and it can be highly structured. All-sky camera images, which are unfortunately not available in the present study, could be used to model the nightglow more precisely. The integrated starlight covers a wide spectrum over all observed wavelengths and is unpolarized. It varies with the time and place and could be recovered with astronomical tools in up-coming studies.

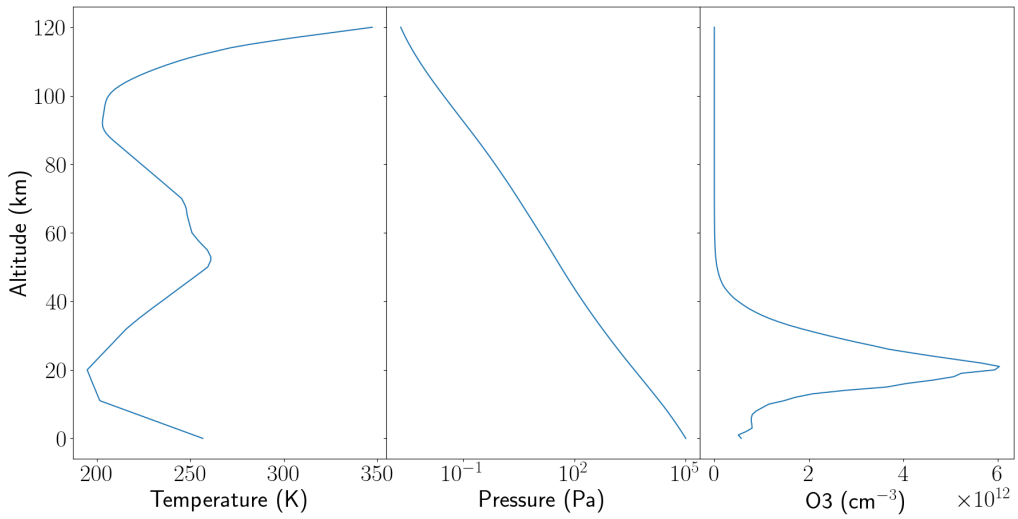

Figure 1: Mid-Latitude night time atmospheric profiles from the 2001 MIPAS model (see text for details). From left to right: temperature [K], pressure [Pa], Ozone number density [cm^{-3}].

For now on, since the absolute values of these contributions cannot be estimated, and also because the absolute radiant flux measured by the instrument is not calibrated, we cannot disentangle the several background contributions from the confrontation of our measurements with the model outputs. Thus, the background contribution may be considered to account for the model uncertainties. These are different for each wavelengths, time and location of observation.

3.1.4 Atmospheric properties

To compute the Rayleigh scattering in the atmosphere, we need different atmospheric parameters. We use the 2001 MIPAS Model Atmospheres (Remedios et al., 2007) up to the lower thermosphere, at 120 km of altitude. It provides the temperature $T(z)$ and pressure $P(z)$ vertical profiles (z is the altitude) as well as an ozone vertical profile. For the present purpose, we use their standard night-time mid-latitude profiles, displayed in Figure 1.

To account for the influence of the aerosols, we consider a Lorenz-Mie scattering model (Lorenz, 1890; Mie, 1908; Born & Wolf, 1999; van de Hulst, 1981). This implies a wide range of input parameters, such as the complex refractive index, the aerosol sizes and their vertical profiles. Three aerosol models are considered in this paper, named 1-low, 2-high and 3-mid, whose parameters are listed in Table 1 (aerosol model names reflect the atmospheric aerosol content). We use complex optical indices from Dubovik et al. (2000) assumed to be the same for all wavelengths considered in this paper. The size distribution $n(\ln(r))$ of the aerosol is supposed to be log-normal,

$$n(ln(r)) = \frac{dN}{d\ln(r)} = \frac{N}{\sqrt{2\pi}\ln(\sigma)} \exp\left(-\frac{\ln^2(r/R)}{2\ln^2(\sigma)}\right), \tag{6}$$

with r the aerosol radius (in µm), N the total number of aerosols, R the mode radius (the radius where the distribution is maximal) and $\ln(\sigma)$ controlling the dispersion of the aerosol sizes around R. Below 12 km altitude, the vertical number density distribution of aerosol $n(z)$ is given by

$$n(z) = n_0 \left[\exp\left(\frac{-z}{H}\right) + \left(\frac{n_B}{n_0}\right)\right], \tag{7}$$

with n_0 the number density at the surface (in cm^{-3}), n_B the background number density (in cm^{-3}) and H the scale height (in m). Above 12 km of altitude, $n(z)$ is set to zero. The values chosen

	Complex refractive index		Size distribution		Vertical number density profile		
Aerosol profile name	Real	Imaginary	R (μm)	$ln(\sigma)$	H (m)	n_0 (cm^{-3})	n_B (cm^{-3})
1-low	1.45	0.0035	0.15	0.29	440	4000	10
2-high	1.61	0.03	0.557	0.266	500	1000	1
3-mid						500	

Table 1: Parameters used to define the aerosol model (see text for details).

Wavelength (nm)	τ_{ray}	τ_{O_3}	τ_{aer} 1-low	τ_{aer} 2-high	τ_{aer} 3-mid
620.0	0.060	0.034	0.060	0.480	0.257
557.7	0.092	0.031	0.074	0.470	0.252
427.8	0.274	0.001	0.115	0.464	0.248
413.0	0.317	0.0004	0.121	0.463	0.248
391.4	0.396	0.0002	0.129	0.461	0.247

Table 2: Optical depths of the atmospheric components for all wavelengths of interest. τ_{ray} is the optical depth of Rayleigh scattering, τ_{O3} is the optical depth of ozone and τ_{aer} is the optical depth of aerosols for the three aerosol models used in this study.

for the above parameters are taken from Jaenicke (1993). In the context of the present paper, we consider these standard aerosol profiles to be sufficient in order to illustrate our purpose. However, in future studies they could be recovered from independent measurements (e.g. LIDAR) or using an inversion scheme in order to best fit polarization data.

Table 2 shows the top-to-bottom optical depth of the different components of the atmosphere model. For Rayleigh scattering, the optical depth increases with the wavelength as expected. For ozone, the optical depth is negligible for short wavelengths (blue and shorter), but not for the green and orange lines. The aerosol optical depths are presented for the three models described in Table 1. We can observe two behaviors depending on the aerosol size distribution. For the model 1-low with an average size of 0.15 μm, the optical depth increases towards shorter wavelengths. At 620 nm, the value is equal to that of Rayleigh scattering by coincidence. However, as the wavelength shortens, the optical depth of aerosol diverges from Rayleigh scattering as dictated by the Ångström law (Ångström, 1929). For model 2-high and 3-mid, the aerosol optical depth is almost constant over all considered wavelengths, in comparison with Rayleigh or the 1-low aerosol case. This comes from the much larger average size used (0.557 μm).

3.1.5 Topographic map

Our model also incorporates the topography around the instrument. It is used for the computation of occultation: when a light beam hits the ground between the emission and the scattering point, its contribution to the light received by the instrument is set to zero. The topographic altitude data are taken from ALOS GLobal Digital Surface Model AW3D30 DSM of the Japan Aerospace Exploration Agency (Tadono et al., 2016). It has a resolution of 30 m, which can be downgraded to any value in order to reduce the computation time. We use here the highest resolution available.

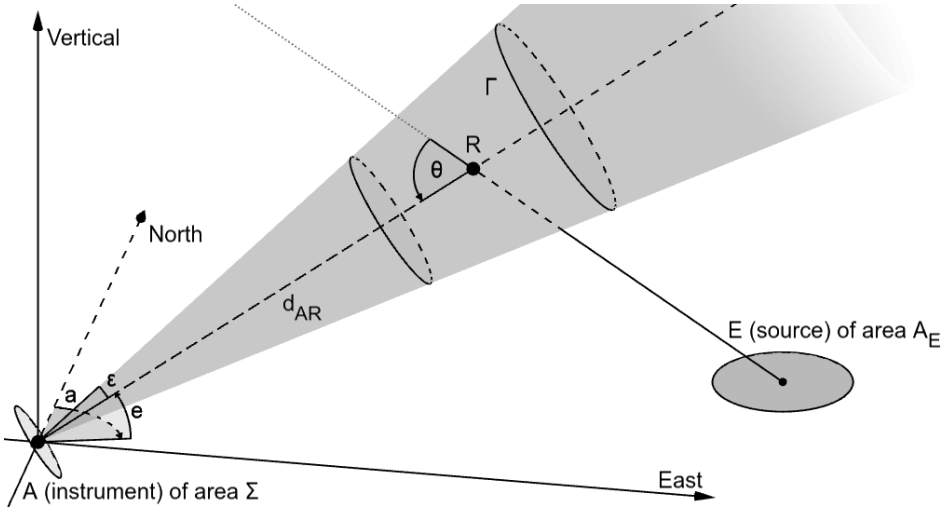

Figure 2: Geometry of the problem for a light source in E of area A_E, a scattering volume (Γ) centered at R and the instrument in A of area Σ and half aperture angle ϵ. The instrument pointing direction is defined by its azimuth a and elevation e. θ is the scattering angle.

3.2 One-dimensional radiative transfer model

We describe here the general algorithm used in POMEROL to compute the scattering of extended sources along the line of sight of the virtual instrument. Figure 3 gives a schematic representation of the process. First, the model loads all the necessary input data (see Section 3.1 for details). It then proceed to compute the light polarization detected by a virtual instrument in this environment. For this, POMEROL is able to compute the polarization of the light coming from a single point source, scattered at a single point along the line of sight and reaching the detector (see Appendix A for details). This computation is then repeated $N_{pix} \times N_{los}$ times, where N_{pix} is the number of pixels in the input emission map and N_{los} the number of bins along the line of sight. For this computation, the Stokes parameters are defined with respect to the scattering plane. They are immediately converted to a global reference frame attached to the virtual instrument such that in all of the following steps, all Stokes parameters of every scattering events are defined consistently (see Appendix A2 for details). This reference frame is defined by the plane attached to the virtual instrument and containing the line of sight which is horizontal in the case of the instrument pointing to the horizon. Q is the quantity of vertical and horizontal polarization, while U represents the polarization oriented at 45°. POMEROL integrates all these contributions together to retrieve the total light reaching the detector and its polarization (G). So this is computed as the double sum of the Stokes parameters over all point sources and along the whole line of sight as:

$$\begin{aligned} I^{total} &= \sum_{sources} \sum_{l.o.s.} I\,, \\ Q^{total} &= \sum_{sources} \sum_{l.o.s.} Q\,, \\ U^{total} &= \sum_{sources} \sum_{l.o.s.} U\,. \end{aligned} \tag{8}$$

The units are again given in nW (see equation 4). One can then use the formulas of equation 5 to retrieve the *DoLP* and *AoLP* as presented in this article. Then, a uniform, isotropic and constant un-polarized light is added to the result to model the background star light and the nightglow (K). Both contribution (G and K) are not inter-calibrated, so the final model M is a linear combination of the two: $M = aG + bK$. The parameters of this linear combination (a and b)

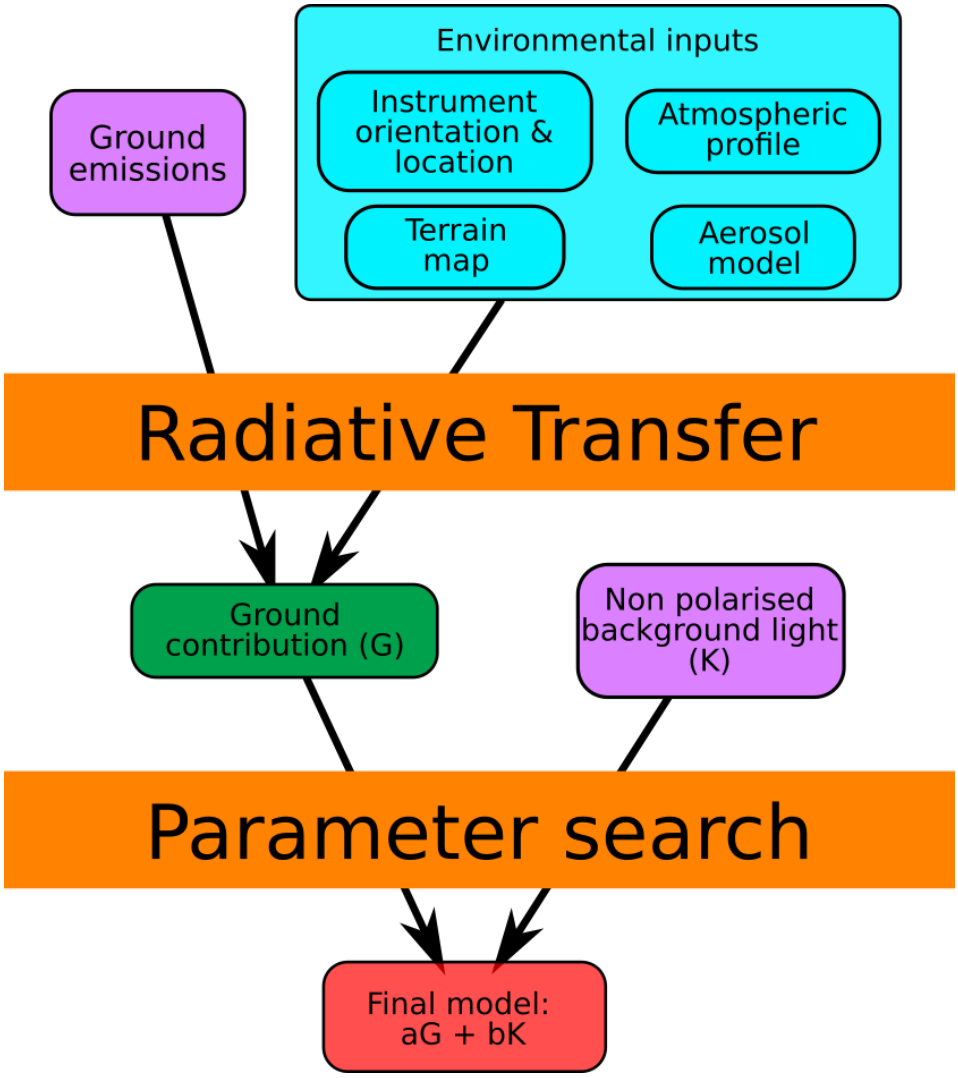

Figure 3: General overview of the POMEROL algorithm. Environmental inputs (in blue) are described in detail in Section 3.1. In pink, both light sources taken into account in the model: sources on the ground which are detected by the virtual instrument via scattering in the atmosphere (G) and the isotropic un-polarized background (K). The final model is given by a linear combination of both contributions (G and K).

are chosen to best fit the measurements of the radiant flux (I). The parameter search does not depend at any point on the polarization. Thus, the addition of the background has only two effects. The first one is to inter-calibrate the model units and the instrument units so that the radiant flux is comparable. This step completely determines a and b. The addition of this un-polarized background has a secondary effect, which is to reduce the model $DoLP$. We note that the parameter search does not take into account the reduced $DoLP$ and does not try to fit the model $DoLP$ to the measurements.

4 Model validation and influence of the parameters

In this section we study:

i) The influence of a localized source on the ground (such as a cities), at several distances from the instrument, and in the absence of any source in the sky ;
ii) The influence of the atmospheric parameters (absorption by O_3, aerosols) for a localized source on the ground;
iii) The effect of a uniform source in the sky, polarized or not, in the absence of any source on the ground.
iv) The domain of validity of the single scattering approximation (in comparison with multiple scattering) by comparing POMEROL outputs with modeling and observations provided by Pust & Shaw (2011).

These reduced configurations have been chosen so as to illustrate the most important factors that impact ground-based polarization measurements. In the following, we present results by means of clockwise almucantars of elevation 45°, the starting direction being the North. The virtual instrument parameters (Σ and ε) correspond to that of the real polarimeter (see Section 3.1.1). In the following series of tests, we use a polarized Lorenz-Mie scattering model for scattering by aerosols (see Section 3.1.4). The comparison between the aerosols models and real data is shown later on in Section 5.1.2. The atmospheric profile used for the tests is the MIPAS standard nighttime mid-latitude profile (see Section 3.1). We show here results at $\lambda = 557.7$ nm (auroral green line, Table 3). For the tests presented in this section, an hypothetical source of arbitrary radiance is considered, such that the wavelength only plays a role in computing atmospheric extinction and scattering coefficients. In the following sections where we present comparison with observations, the input emission maps are integrated over the visible spectrum (see Section 3.1.2).

4.1 Influence of a localized source on the ground in absence of any source in the sky.

We consider an isotropic point source on the ground of radiance 100 nW/m^2/sr, at different distances d_{AE} away South of the virtual instrument. The purpose of this arbitrary setup is only to showcase the influence of a point source on the ground at different distances from the instrument. Thus, the radiance is arbitrary and do not correspond to any real world values, but the distances are chosen to be representative of a real environment (between 1 and 100 km). There is no mountain obstruction. The ground surface takes the Earth curvature into account. Only Rayleigh scattering and ozone absorption are taken into account, no aerosols are present in the atmosphere. The ozone is taken into account through its number density vertical profile (Figure 1) and its absorption cross sections as a function of the wavelength (Figure A1). For a source located 100 km away from the observation point, the ozone decreases the measured radiant flux by less than 3%. There is no effect on the *AoLP* since this angle depends only on the scattering plane (defined by the emission and scattering direction). The effect on the *DoLP* is smaller than 0.4%, and the closer the source, the lower the effects. More complex sources than a point may slightly increase these values. From now on, we take into account the impact of O_3.

In Figure 4, we show the polarization results for $d_{AE} = 1, 5, 10, 50$ and 100 km. In all such figures, the upper panel shows the radiant flux measured by the virtual instrument, representing the energy per unit time on the collector, the middle panel shows the *DoLP* and the lower panel the *AoLP*.

The further the source, the lower the measured radiant flux. However, the effect is not merely a decrease as d_{AE}^{-2}, because the source illuminates points at all altitudes along the line of sight that are integrated on the virtual instrument. Moreover, the light parameters change during its crossing into the atmosphere from the source to the line of sight, and along the line of sight. As seen in Figure 1, the concentration in ozone peaks at about 20 km. As an example, the decreasing factor between a source lying at 1 and 10 km is about 25 (and not 10^2 if only the effects of the distance were considered). It becomes approximately 5 000 (and not 10^4) with a source at 100 km compared to 1 km. Because of the exponential decrease of the atmospheric pressure with the altitude, this effect is less important when the source moves away from the polarimeter. However, in all cases, the radiant flux is maximum in the Southern direction, i.e. toward the source.

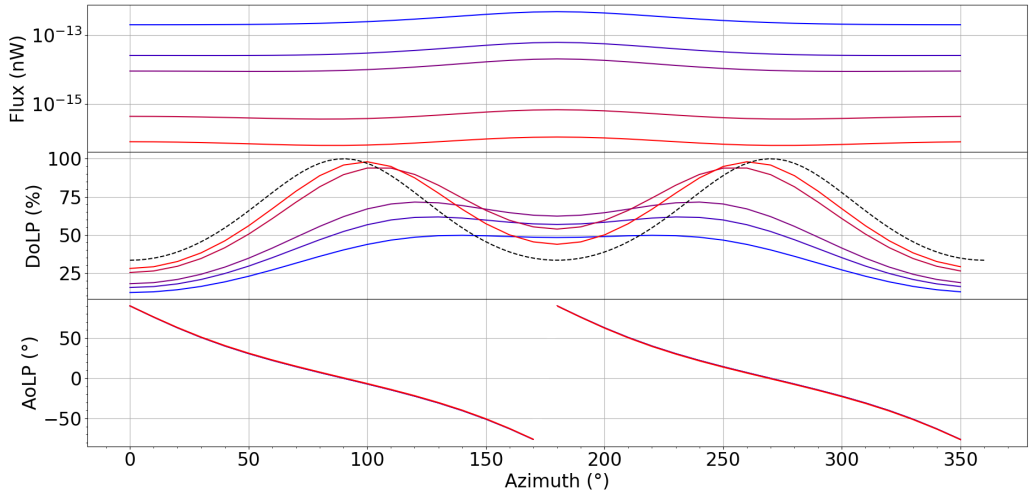

Figure 4: Almucantar for $e = 45°$, for a point source on ground, on a flat Earth surface, South of the instrument at varying distances d_{AE} (with no aerosols). Upper panel: measured radiant flux [nW] for a source of radiance 100 $nW/m^2/sr$. Middle panel : DoLP [%]. Lower panel: AoLP [°]. From blue to red: $d_{AE} = 1, 5, 10, 50, 100$ km. In the upper panel, the highest value (in blue) corresponds to the closest source position and the lowest value (in red) to the most distant point source. Similarly, in the middle panel, the most distant point source has two very marked maxima (in red) while the closest is the flattest (in blue). The dashed line in the middle panel corresponds to a theoretical case for a source at infinite distance.

Geometrically, for a single point source and a given line of sight, the *AoLP* of every scattering point is the same. In this particular case, we do not have to use the I, Q and U notation (equations 5). The total *DoLP* integrated along the line of sight is an average of the $DoLP(\theta_i)$ of each scattering points i weighted by the scattered radiant flux F_i as

$$DoLP = \frac{\sum_i F_i DoLP_i(\theta_i)}{\sum_i F_i}, \tag{9}$$

where θ_i is the scattering angle at point i, F_i follows equations (A1) and DoLP_i equation (A25). In the limit of a source infinitely far away from the instrument (on a flat surface), all paths from the source to the instrument are parallel. Thus, the scattering angle is the same everywhere on a given line of sight. The total DoLP measured by the virtual instrument should then follow equation (A25) (dashed line in Figure 4, middle) since there is no aerosols in this case. When looking eastwards and westwards, the value of the DoLP reaches 100% as expected from the theory. When the source gets closer to the virtual instrument, each point along the line of sight has a different scattering angle, which smooths the variations along the almucantar. On a flat surface, the *AoLP* is the same whatever the distance from the source (Figure 4, bottom).

4.2 Influence of the aerosols for a localized source on the ground

The aerosols are taken into account through their number density vertical profiles and their cross sections (Table 1). The aerosol cross section depends on the wavelength as computed using Lorenz-Mie theory (Lorenz, 1890; Mie, 1908; Born & Wolf, 1999). For the sake of simplicity, we consider the aerosol refractive index to be the same for all wavelengths. A variation of the refractive index with wavelength could be taken into account, but is out of the scope of the present study.

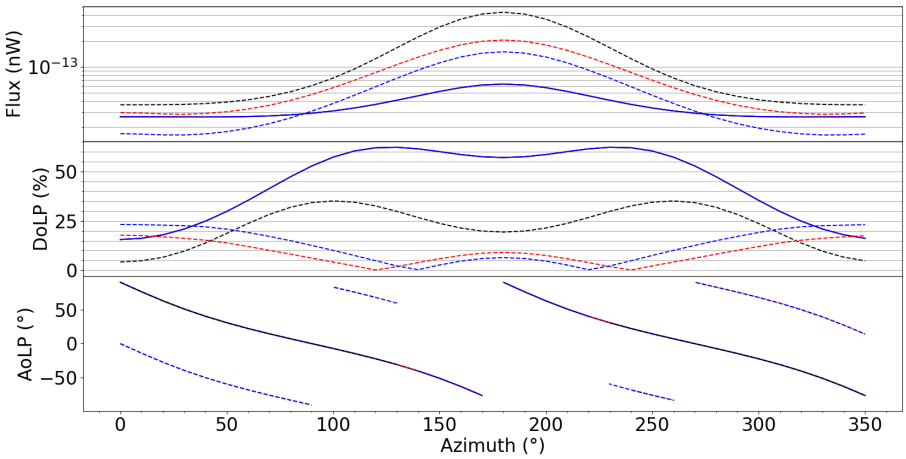

Figure 5: Almucantar for $e = 45°$, for different aerosol profiles. A point source is located 5 km South of the instrument. The continuous line is the case without aerosols (similar to Figure 4). The dashed lines correspond to three different aerosol models listed in Table 1: 1-low (black), 2-high (blue) and 3-mid (red).

In order to illustrate the effect of the aerosols, we consider three different profiles listed in Table 1: 1-low, 2-high, 3-mid. The impact of the aerosol profiles is drastic, but not straightforward to interpret. It is illustrated in Figure 5, for a point source located 5 km South from the observation point. With the 1-low model (lowest aerosol contribution), the radiant flux is increased by 600% (with respect to the case with no aerosols) when pointing above the source, and by 40% in the opposite direction. Using the 2-high profile (highest aerosols contribution), the radiant flux is increased by 150% when pointing above the source, and decreased by 40% in the opposite direction. With the 2-mid model, the radiant flux above the source increases by 120%, against 10% in the opposite direction. The ratio of the maximum to minimum radiant flux along the almucantar is in all cases amplified by the presence of aerosols.

For an increasing aerosol contribution, the *DoLP* decreases in the direction of the source. With the 1-low model, it decreases by about 50%, with the two maxima along the almucantar still present. The *AoLP* does not change since the aerosol radius is small compared to the wavelength, and the polarization direction is the same as for Rayleigh scattering ($AoLP^{ray}$). However, when the aerosol size is large compared to the wavelength (2-high and 3-mid), the *DoLP* behavior changes drastically, with a maximum at about 25% when pointing away from the source. The *AoLP* is shifted by 90° when pointing away from the source due to larger aerosol size, while it is the same as $AoLP^{ray}$ when pointing towards the source. The impact of aerosols on the virtual instrument observations is complex. They may for instance either increase or decrease the intensity depending on their size or on the scattering angle. They do therefore play a major role. Spanning all possible aerosol models is not a crucial point for this study, and we limit ourselves to the three models presented here.

4.3 Influence of the skylight with different polarization parameters

We document here the effect of a simple skylight (nightglow and/or integrated star light). It is modeled as an infinitely thin uniform sky emission of arbitrary intensity at 110 km of altitude. The model computes the sum of the non scattered light and the single Rayleigh scattered light measured by the instrument. In order to prepare for further auroral studies (out of the scope of this article), we allow this emission to be polarized (Bommier et al., 2011). Figure 6 shows

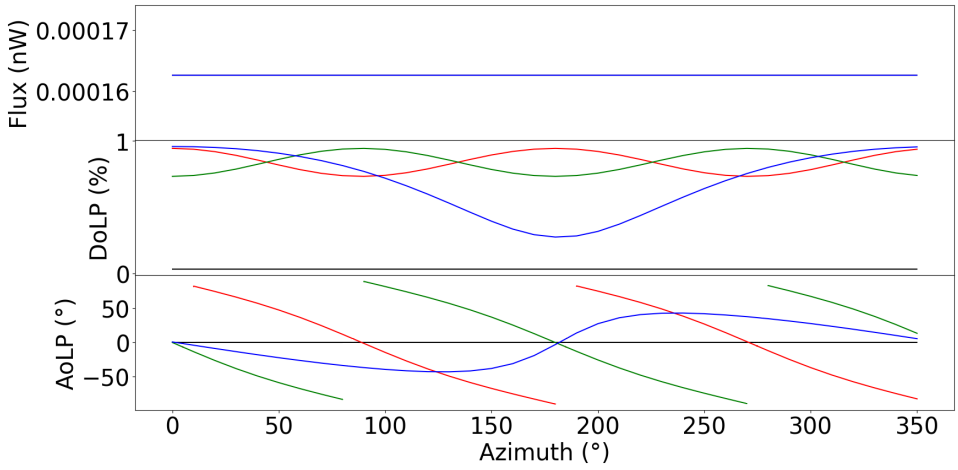

Figure 6: Polarization parameters for an almucantar at $e = 45°$ in the presence of an isotropic skylight of radiance taken at 100 nW/m^2/sr at 557.7 nm. No aerosols are present in the model. The direct radiant flux is taken into account, with different polarization parameters. No polarization of the skylights (black line), with a 1% polarization along the East-West (red) and North-South (green) directions, and along the magnetic field direction (blue).

the model outputs over an almucantar (with no aerosols), for a nightglow either unpolarized, or polarized with a $DoLP = p_{source} = 1\%$ (arbitrary choice) along several directions: East-West (EW), North-South (NS) or along the magnetic field (B). For this last case, the instrument is positioned at latitude 45.2123°N and longitude 5.9369°E and we use the CHAOS-6 internal magnetic field model (Finlay et al., 2016) evaluated in 2019. The atmospheric profile described in Section 3.1 is used. As the background skylight is isotropic, the measured radiant flux does not change over an almucantar.

In cases where the nightglow is polarized, the *DoLP* depends on the angle α between the line of sight and the polarization direction, as $DoLP = p_0 + p_1 \sin\alpha$. For the EW and NS cases, $p_0 \approx 0.85 p_{source}$ and $p_1 \approx 0.1 p_{source}$. When the nightglow is polarized along the magnetic field lines, the behaviour is much different as the lines are close to vertical, with $p_0 \approx 0.6 p_{source}$ and $p_1 \approx 0.3 p_{source}$. For a uniform sky emission and in the absence of other sources, Figure 6 shows that the polarization from Rayleigh scattering in the atmosphere is relatively small compared to the polarization of the non scattered light. Thus, in this simple configuration, any polarized source in the sky with a *DoLP* higher than the instrument noise level should be detectable.

The *AoLP* (lower panel) for the unpolarized nightglow emission (continuous black line) is undefined (it is set to zero by default, with no physical meaning). The EW and NS cases show an *AoLP* regularly rotating over all 360° with the same behavior, but shifted in azimuth by 90°. As expected from the *DoLP* definition, the maximum *DoLP* corresponds to a 90° *AoLP*. When the nightglow polarization direction is aligned along the magnetic field, the magnitude of the *AoLP* variations along an almucantar is significantly weaker, within ±40°, which led Bosse et al. (2020) to reject this single source as the origin of the measured polarization of auroral lights.

4.4 On the impact of multiple scattering

The model described here does not consider the effects of multiple scattering. We recall that the main goal of this approach is to test the feasibility of night-time polarization measure-

ments and modelisation, and not to develop a new state of the art radiative transfer code. However, these effects can not be neglected, in particular at the shortest wavelengths, and we discuss here their impact. The literature on the atmospheric polarization is already large, both in term of observation and modeling. The reader may refer to the seminal work of Hovenier (1971) and Hansen & Hovenier (1971) on the modelisation of terrestrial and planetary clouds illuminated by the sun. It is known that single scattering models of the atmosphere miss part of the measured polarization properties, especially at short wavelengths. The limitations of the single scattering approach was for instance addressed by Hansen & Travis (1974) who showed the early improvements brought by multiple scattering (MS). Polarization properties are not erased by MS (Hansen, 1971). Generally, in comparison with single scattering, MS tends to enhance the radiant flux and reduce the *DoLP*, with relative effects that depend on the optical depth, the solar elevation and the wavelength (Hovenier, 1971). An order of magnitude of the MS effect is proposed for instance by Staude (1975) who mentioned an increase in the radiant flux ranging from 10 to 45%, and a drop in the *DoLP* from 5 to 20%, depending on the optical depth. It is acknowledged that simply using a scaling factor to accurately match *DoLP* and radiant flux observations with single scattering is over-simplistic (Hansen & Hovenier, 1971). In atmospheric optics, the SSA is more of an issue towards short wavelengths (e.g. Hovenier, 1971), while it can give decent predictions for red and longer wavelengths. There are several approaches to polarized MS, such as adding–doubling methods with several levels of refinement, Monte-Carlo methods, etc. (de Haan et al., 1987; King, 1986; Ramella-Roman et al., 2005). For a review of multiple scattering of waves from the theoretical perspective, see for example Lax (1951).

Several studies addressed the comparison between single and multiple scattering of polarized light in the atmosphere. One can cite Evans & Stephens (1991), but also a series of balloon experiments (Herman et al., 1986; Santer et al., 1988), which interpretation was first based on a single scattering approach, and later on refined with MS. Ougolnikov & Maslov (2002), followed by Ugolnikov et al. (2004) proposed a thorough study on the impact of MS as a function of the wavelength in the visible range. They conclude to a radiant flux contribution from single scattering ranging from about 55% in the blue to over 80% in the red (slightly less than theoretical estimates). A comprehensive study over a wide range of wavelengths and zenith angles can also be found in Pust & Shaw (2011) (mentioned as PS11 hereafter), in various aerosols conditions.

However, the configuration of our experiment significantly differs with most of the already documented work. PS11 for instance evaluate the polarization of the solar light scattered in the atmosphere. They do not study the *AoLP*, and only provide measurements of the maximum *DoLP*, i.e. in a direction at approximately 90° from the Sun direction. Many of such studies also consider the rising Sun only. In our case, we consider a mixture of sources, either extended or localised, during the night-time, and observed over a multiplicity of angles.

Then, because our study constitutes a first approach to a fully new principle of night-time atmospheric observations, we wish to keep our set-up as simple as possible, although realistic, and we do not account for MS in this prototype version of the POMEROL model. Its effect is out of the scope of the present work, and should constitute a dedicated future study. As we will see later, already a large part of our night-time measurements can be interpreted in the single scattering approximation, which means that the SSA can already catch a great part of the phenomenon we are dealing with. This is particularly true not only for the *DoLP* profiles along one almucantar, but also for the *AoLP* data, a quantity that is almost never considered in the literature. Meanwhile, we provide below an estimate of the uncertainty level associated with this limitation of our model, by presenting comparisons of POMEROL with previously published observations and MS model predictions from PS11.

These authors studied the output of the MODTRAN-P model (e.g. Berk et al., 2014), accounting or not for the effect of MS. Their model was tested against measurements corresponding to various aerosol contents: a clear day with low aerosol content, another day following a forest fire with high aerosol content and finally shortly after the fire, a day with moderate aerosol content. For each day, they measured the *DoLP* of the sky with an all-sky camera at different wave-

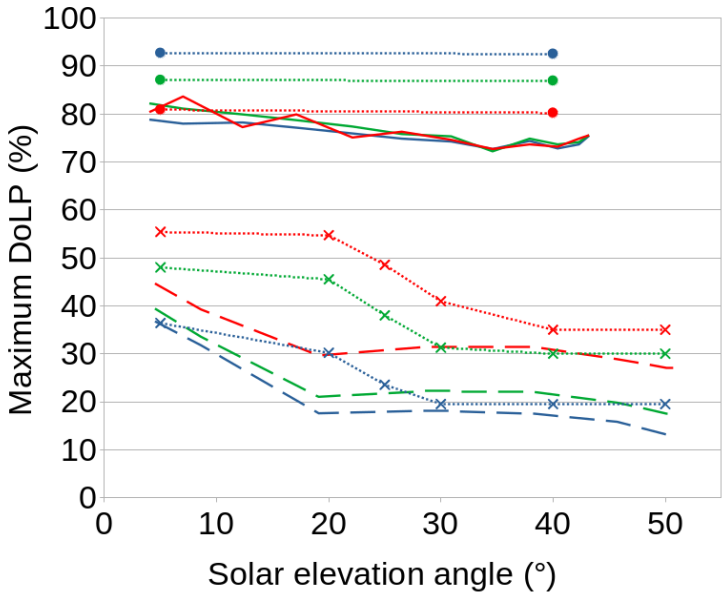

Figure 7: Maximum *DoLP* found over the sky as a function of solar elevation angle at three wavelengths: 630 nm (red), 530 nm (green) and 450 nm (blue). Observations from PS11 are shown in plain lines (resp. dashed lines) for a low (resp. high) aerosols content. Predictions from POMEROL are shown in dotted lines with circle (resp. crosses) for low (resp. high) aerosols content.

lengths, and compared the maximum *DoLP* found in the sky with their model prediction, as a function of solar elevation. They found that single scattering overestimates the *DoLP*, while it is under-predicted by unpolarized MS. However, in low aerosol conditions, the SSA is sufficient to reproduce their data for long wavelength (> 630 nm).

We report their measurements in Figure 7 at three representative wavelengths (630, 530 and 450 nm) and for the two extreme days with low and high aerosol content. We see a decrease of the maximum *DoLP* with increasing solar elevation. This effect is more important for high aerosols conditions and stronger for large elevations and short wavelengths. To reproduce the above configuration with POMEROL, we set a point source at a given elevation representing the Sun, and compute the *DoLP* for each observation direction in the sky. We then take the maximum *DoLP*, which is always found in a direction around 90° of the Sun for low aerosol contents. No ground reflections are taken into account. We use the 1-low aerosol profile for the day before the fire, and the 2-high aerosol profile for the time just after the fire. Note that the vertical concentration profiles have been tweaked so that the optical depth matches that of the aerosol profiles considered by PS11.

In the first case with low aerosol content, POMEROL overestimates the maximum *DoLP* for short wavelengths: at 450 nm, the modeled *DoLP* is $\sim 20\%$ too high (in relative values). At 630 nm however, single scattering predictions from POMEROL are much closer to the observations, although our model does not reproduce the $\sim 10\%$ relative increase seen in the maximum *DoLP* for low elevation angles. This result is overall consistent with the behavior of MODTRAN-P by PS11 in similar conditions: single scattering model with a low aerosol content (see Figure 8). The several low aerosol models considered by PS11 give a hint of the sensitivity to this parameter, with a spread of the predicted maximum *DoLP* that ranges from 5% to 8% from 450 to 630 nm (i.e. less than $\sim 10\%$ in relative values).

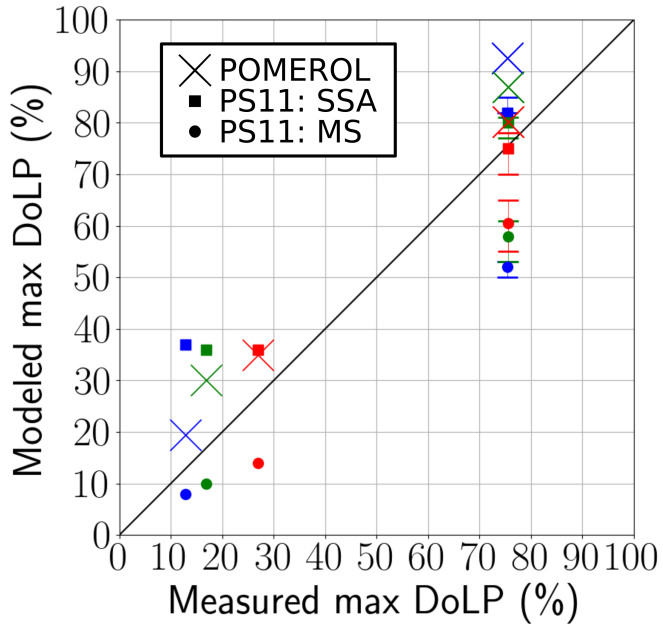

Figure 8: Comparison of POMEROL and MODTRAN-P maximum *DoLP* with the PS11 observations at maximum solar elevation, at three wavelengths: 630 nm (red), 530 nm (green) and 450 nm (blue). The group of points with *DoLP* $<$ 40% correspond to a high aerosol content, while symbols in the upper right quadran correspond to a low aerosol content. Crosses represent the result of POMEROL. Single (resp. multiple) scattering predictions obtained with MODTRAN-P by PS11 are indicated with squares (resp. circles). The spread within the several low aerosol contents investigated by the authors is indicated by errorbars.

In the case with high aerosol content the observed maximum *DoLP* decreases from around 45% at low solar elevation down to $\sim$ 30% at 630 nm and it decreases frrom 35% to 15% at 450 nm for solar elevation above 20°. This trend is overall recovered with POMEROL that shows a net decrease in the *DoLP* at solar elevation above 20° in all wavelength (see Figure 7). At 450 nm, the maximum *DoLP* is well reproduced at high and low solar elevation, but is overestimated in between. At 630 nm and 530 nm, the *DoLP* is overestimated for all angles, with larger differences around 20° solar elevation. In comparison, the single-scattering model predictions by PS11 overestimate the maximum *DoLP* by a factor as large as $\sim$ 2 at 450 nm (see Figure 8). Here again the difference with our model might come from distinct aerosol profiles used in both studies.

As shown with the above example, POMEROL tends to overestimate the *DoLP* for a day-like environment, i.e. a single point source at infinity. This effect is sensitive to the aerosol profile, the wavelength and whether or not MS is considered in PS11. The benefits that we could gain by implementing MS is expected to be larger at short wavelengths. Meanwhile, we notice that the above test situation differs from our experimental environment in several ways. During the day, the Sun is approximated as a single point source because it dominates other light sources. By night on the contrary, light pollution from urban lightning and spread emissions from the integrated star light and airglow are mixed all together. In this case, the measured polarization depends heavily on the relative contributions of the different sources rather than on the absolute contribution of each one. We thus expect MS impact on the *DoLP* and *AoLP* to decrease for nighttime scenarios.

Name	Wavelength (nm)	Instrumental width (nm)	Atmospheric source	Layer
Orange	620	2	OH	High Mesosphere ($<$ 80 km)
Green	557.7	10	O	Thermosphere (110 km)
Blue	427.8	10	N_2^+	Ionosphere (90 km)
Turquoise	413	10	O_2	Mesosphere ($<$ 80 km)
Purple	391.4	10	N_2^+	Ionosphere (85 km)

Table 3: List of emission lines observed during the January, 2021 campaign (see text). All emissions are present in the light pollution spectrum.

MS can not be neglected in most cases, particularly at short wavelengths ($\approx <$ 600 nm). The conditions of our experiment corresponds to a low aerosol content. In this case, only a moderate sensitivity to the source angle has been reported, and we can expect MS to decrease the *DoLP* by at most about 20% at 450 nm, and less for longer wavelengths. MS is thus expected to result in a more isotropic contribution than single scattering, with a lower *DoLP*. For the sake of simplicity, we then incorporate its effect together with that of the uniform, isotropic and unpolarized emission in the sky (both tend to reduce the *DoLP* and increase the radiant flux). One consequence of this coarse approximation is that we cannot isolate unambiguously the signature of the airglow and/or starlights. Still, this parsimonious approach appears to be enough to account for a significant part of our observations for wavelengths down to the blue line at 427.8 nm, as we shall see later.

5 Comparison with geophysical measurements at mid-latitude

In order to validate our model, we performed a series of observations in the French Alps. In the following, we focus on the night from 19 to 20 January, 2021 when the moon was down (below -10° elevation during the whole observation). The latitude is 45.2123° and longitude 5.9369°. The altitude is 770 m. The nearest city is Grenoble 15 km away with downtown at an azimuth of 260°. However, the valleys around this bright city produce also some light pollution. Figure 9 shows the geographical configuration with lines of constant elevation at 500 m, 1000 m and 2000 m.

The light pollution was clearly visible with the naked eyes. At the time of the observations, the snow was covering the ground above about 500 m elevation. The altitudes below $h \approx 1500$ m are mostly covered with forests in the mountains which lowers the albedo significantly, even though some snow remains on the trees. The air temperature was below 0°C all over the surrounding area, and reached about -5°C at the point of observation. The modeling below takes the relief into account (see Section 3.1). We could observe simultaneously five wavelengths, summarized in Table 3: three of them concern emissions bands emitted in the upper atmosphere, either in the thermosphere (green, due to the O^{1S} excitation state) or in the thermosphere (blue and purple, due to the 1^{st} N_2^+ negative band). The "orange" band around 620 nm is not present in the thermosphere, but is emitted in the mesosphere by OH(5-0) and OH(9-3), though with a relatively lower radiant flux (Broadfoot & Kendall, 1968; Bellisario et al., 2014, 2020). Finally, the turquoise line can be produced by Herzberg and Chamberlain O_2 lines and/or ground light pollution. The former indeed induce spectral lines of weak intensity (Broadfoot & Kendall, 1968; Leinert et al., 1998), while the latter, which we account for, might be related to the presence of *Hg* in city lights. The two contribution are likely weak, and the main *Hg* line falls outside the filter bandwidth.

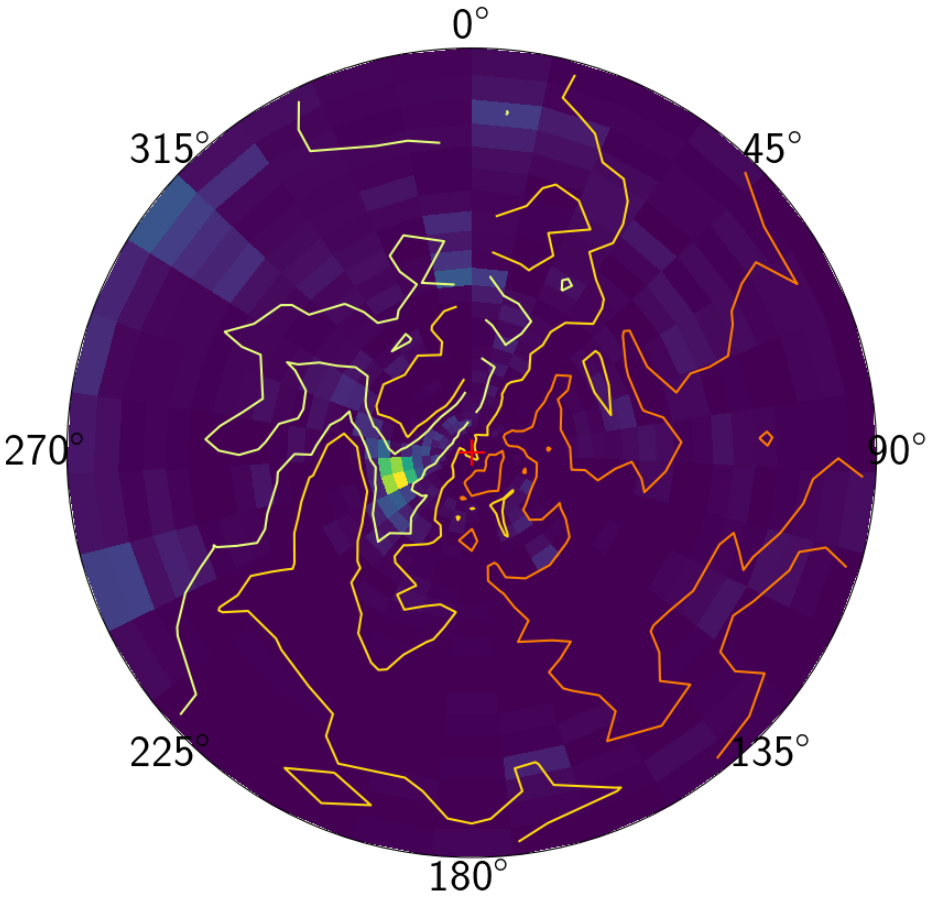

Figure 9: Input emission map and contour of the elevation map for altitudes 500 m (white), 1000 m (yellow) and 2000 m (orange). The instrument is at the center of the map (red cross). Grenoble is the bright emission west to the instrument. The map covers 100 km around the instrument.

We show below the results of an almucantar at a constant elevation $e = 45^\circ$ from 1:18 UT to 3:35 UT taken with the real instruments and compared to the virtual one (i.e. the modeling). We rotate clockwise from North to the East and back to North with 10° increments in azimuth. At each step in azimuth, we record the radiant flux, *DoLP* and *AoLP* during about 1'30". We recall that our instrument provides the relative (uncalibrated) measurements of the radiant flux, and the calibrated *DoLP* and *AoLP*. The orientation angles e and a are set using stars as references, together with a compass (to help on the increments in azimuth) and an inclinometer (for the elevation). We consider the accuracy to be of the order of $\pm 2^\circ$.

We focus first on a single wavelength (the green line, see Section 5.1) for which we detail our analysis of the observations. We next discuss the full picture in Section 5.2.

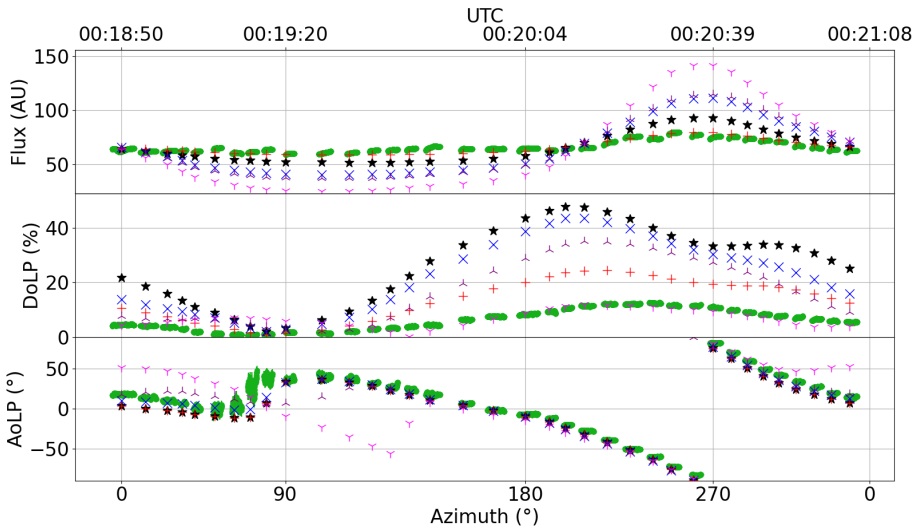

Figure 10: Comparison between model outputs and observational data. Measured data are shown in green, the width of the lines indicating the errorbars (for their computation, we refer to Bosse et al., 2020). Errors on the azimuth due to the pointing direction are of the order of a few degrees (not shown). The other symbols indicate the model output for a ground light pollution map (see text for details). Several aerosol profiles are considered. (see Table 1): without aerosols nor background lights (black ★); without aerosols and with background lights adjusted to fit the radiant flux variations (red +); without background lights and with aerosols model 1-low (blue ×), 2-high (magenta ᵞ) and 3-mid (purple ⅄). Abscissa are given as the pointing direction under the bottom panel (azimuth where 0 is North, 90 is East) and the corresponding time in UTC format above the top panel.

5.1 Model predictions versus observations in the green line

Figure 10 shows an almucantar in the green line. The radiant flux maximizes above downtown Grenoble ($a = 260°$, this is clearer in Figure 12). In the theoretical case of a point source, the *DoLP* maximizes at $\pm 90°$ of the direction of this point (see Section 4 and Figure 4). Here, the *DoLP* shows a single maximum near 240° in azimuth, illustrating the influence of an extended pollution source. The value of its measured maximum is around 12%. The *AoLP* rotates regularly with a behaviour very similar to that of a point source on the ground westward with respect to the instrument.

5.1.1 In the absence of aerosols and background skylight

We first run our POMEROL model with the light pollution as single input (i.e. with neither aerosol nor natural background skylight). We use a ground emission map composed of 1000 pixels mapping an area of 100 km radius around the instrument. The elevation map covering the same area is used to model the mountain obstructions, with a 30 m resolution. Note that the emission maps are not intercalibrated with our instrument, so that the units for the radiant fluxes are arbitrary. The ozone is taken into account, although its effect remains small. The results are shown in Figure 10 (black stars). Both the modeled and measured radiant fluxes peak around the same azimuth (260°). However, the radiant flux variations along one almucantar are significantly larger for the model: the maximum radiant flux is 110% higher than the minimum for the model, with respect to only 43% for the measurement.

The modeled *DoLP* reaches 47% at its maximum around 200° azimuth, about 4 times higher than the highest measured *DoLP*, and is offset by 40° in azimuth. A second local maximum at 300° azimuth is also present in the model, and absent from the measurements. Two maxima in the *DoLP* are indeed expected for a point source (see Figure 4) and are due to the scattering in the first few kilometers of atmosphere. Here it is smoothed out because of the multiple light sources and the occultation from the mountains. This feature is not present in the data and may hint that the model overestimates the scattering below 10 km.

The modeled *AoLP* is very similar to the measurement, showing the same rotation pattern at almost the same angles, except around 90° in azimuth (i.e. pointing away from Grenoble). This difference can be explained by the poor quality of the data in this direction where the radiant flux is minimal and the *DoLP* close to zero, inducing large uncertainties on the *AoLP* measurements (see Bosse et al., 2020).

This first simple approach does not take into account one or more additional sources. We will now show the effects of introducing either a natural background light or the aerosols.

5.1.2 Impacts of aerosols and background skylight

The fact that the model overestimates the radiant flux variations and the *DoLP* in the case above is an indication that non-polarized (or little-polarized) additional sources must be taken into account. Such sources exist naturally: they are the nightglow and the integrated star light. This trend can also be due to the lack of multiple scattering in the model (see Section 4.4). The exact contributions of those effects is delicate to evaluate at this point, so we fit them as a whole called a *background skylight* in such a way that the relative variations of the modeled radiant flux match the measured ones. This method constitutes therefore an indirect estimate of this background skylight (see red + in Figure 10). Here, it is considered constant, isotropic and unpolarized (these approximations could be reconsidered in the future by estimating each contribution from independent measurements or more accurate models, see Section 3.1.3). Averaged over an almucantar, this results in approximately doubling the total radiant flux received by the instrument. This is not visible in Figure 10 because of the Arbitrary Unit radiant flux scale. As expected, the *DoLP* is decreased in any direction by about 50%, peaking at 25% around 220° in azimuth. The two maxima in the modeled *DoLP* over one almucantar are still present, although the secondary maximum appears attenuated. The *AoLP* is unchanged in comparison with the previous case with no background sky, which is expected since the natural background is not polarized.

We now turn to a case with no background skylight, but with the aerosol polarized models included (see Section 3.1.4). The amplitude of the modeled radiant flux variation along the almucantar become larger, whatever the aerosol model, as seen with the synthetic case in Figure 5. The higher the aerosol contribution, the higher the radiant flux variations. The modeled *DoLP* decreases when the aerosol contribution increases, so that it is possible to find a model (2-high: magenta γ) that matches the measured *DoLP*. However, this makes the modeled *AoLP* depart from the measurements, so that it is not possible to find a set of aerosol parameters that allows fitting the measured radiant flux, *AoLP* and *DoLP* at once.

5.2 Comparison of the observations and the modeling in five wavelengths.

From the results presented above, we deduce that even though both additional sources (background and aerosols) significantly affect the polarization parameters, none of them reproduce the measurements alone. We consider below the model predictions for a combination of those two contributions. We first have to choose an aerosol profile. We use the 1-low aerosol model, as it fits best the measurements when combining with background skylight. It could already be intuited from Figure 10 as the 1-low profile affects less the *AoLP* than the other ones. This choice is also coherent as we observe in the Alps at an altitude where the air is very clean. We show hereafter model outputs with this aerosol profile together with a natural background skylight. At all

wavelengths, the modeled radiant flux is the highest in the direction of the city of Grenoble, and the model predictions for the *AoLP* convincingly fit the observed values (see Figures 12 to 14).

The magnitude of the signal from the ground is likely very small in the purple (391.4 nm) and turquoise (413 nm), because in these wavelengths the radiant flux of city lights is in average very weak (see for instance the spectral analysis of Fig. 6 in Bosse et al. (2020) and references herein). The *DoLP* observed for almucantars in these two lines are therefore associated with large error bars. This in turn also affects the uncertainty level for the *AoLP*. The changes of their *DoLPs* with the azimuth appear rather flat, but are also less tightly constrained. Combined with the stronger limitation of the single scattering approach towards short wavelengths, it explains that the model fails at predicting the low values of the *DoLP* observed in the direction of Grenoble at these two wavelengths. Furthermore, ground emissions maps are less sensitive in these wavelengths (Miller et al., 2013), so that the map used in the model might also differ from the real emissions.

Examination of Figure 8 shows that, without any contribution from the background or aerosols, significantly larger values of the *DoLP* are modeled in the green line (557.7 nm). The blue (427 nm) and the orange lines (620 nm) behave similarly. For these three wavelengths, the measured radiant fluxes are fitted when adding the 1-low aerosol model and respectively 114% (Figure 12), 213% (Figure 13) and 43% (Figure 11) of natural background radiant flux (integrated star light and/or nightglow, plus the effect of MS). The percentages are calculated with respect to the maximum radiant flux measured by the instrument around azimuth $a = 260^\circ$. Interestingly, for these three colours we now reproduce also the minima and maxima of the observed *DoLP* along one almucantar, without adding any further complexity to the model. If slight discrepancies remain for the shape of $DoLP(a)$ between the model and measurements for the blue line, this characteristic is very convincingly reproduced by the model in the green and orange lines.

It is striking that we manage to replicate these observations with our model in three different wavelengths simultaneously, as they are affected differently by light pollution, the natural background from the sky, not speaking of MS. Indeed, there exist some orange emissions in the star light and in the mesospheric nightglow (Bellisario et al., 2014, 2020). The green and the blue lines exist both in the stellar light and the natural nightglow originating in thermospheric / ionospheric emissions. From Broadfoot & Kendall (1968), the orange is the tiniest of the three. The blue in the urban light spectrum is much dimmer than the green or the orange. These considerations are compatible with our results.

Finally, the misfit in the *DoLP* observed for shorter wavelengths (turquoise and purple) might require adjusted aerosol profiles (see e.g. Bergstrom et al., 2003, Figure 3). For example a different size distribution which would influence differently the shorter and the longer wavelengths. This would demand a thorough study of aerosols contribution, which is out of the scope of this paper. It is also likely related to the stronger impact of MS towards short wavelengths (see Section 4.4).

6 Discussion

We have presented in this study a polarized radiative transfer model in the single scattering approximation, which can account for a spread light pollution from the ground (including the surrounding topography), natural skylights (from stars or the nightglow) and the effect of aerosols. To our knowledge, it is the first time that such a radiative transfer code, that combines Rayleigh and Lorenz-Mie scattering, is applied to answer the question of the nightlight and its polarization. We have confronted this model to measurements performed at mid-latitudes in the French Alps in five different wavelengths, either within or outside the lines of emissions for the natural nightglow. We obtain a convincing comparison between the model outputs and the observations of the relative radiant flux, degree and angle of the linear polarization in the three wavelengths with the highest signal-to-noise ratio (green, orange and blue lines).

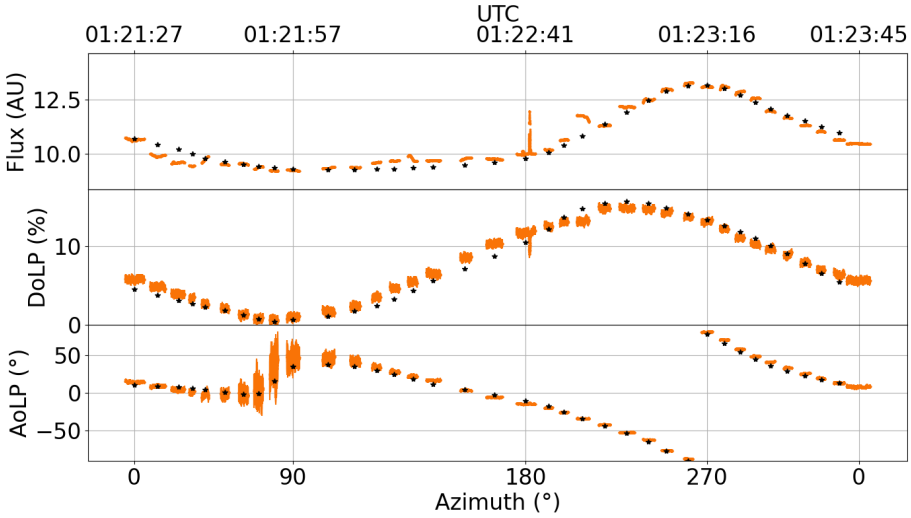

Figure 11: Almucantar in the orange line (620 nm). Measured data are shown in orange, the width of the lines indicating the errorbars. Errors on the azimuth due to the pointing direction are of the order of a few degrees (not shown). Model predictions (black stars) are obtained with the 1-low aerosol profile plus an unpolarized, isotropic background skylight adjusted so as to fit the radiant flux (see text).

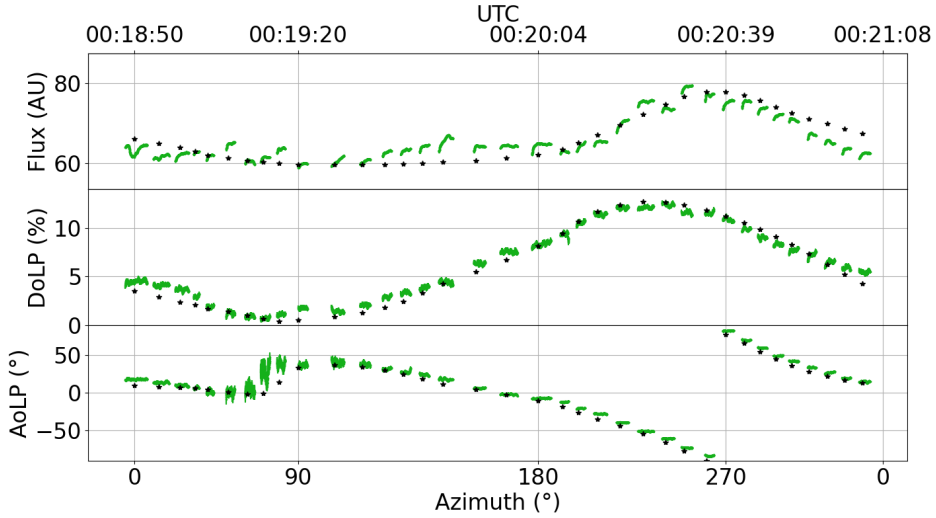

Figure 12: Same as Figure 11 for the green line.

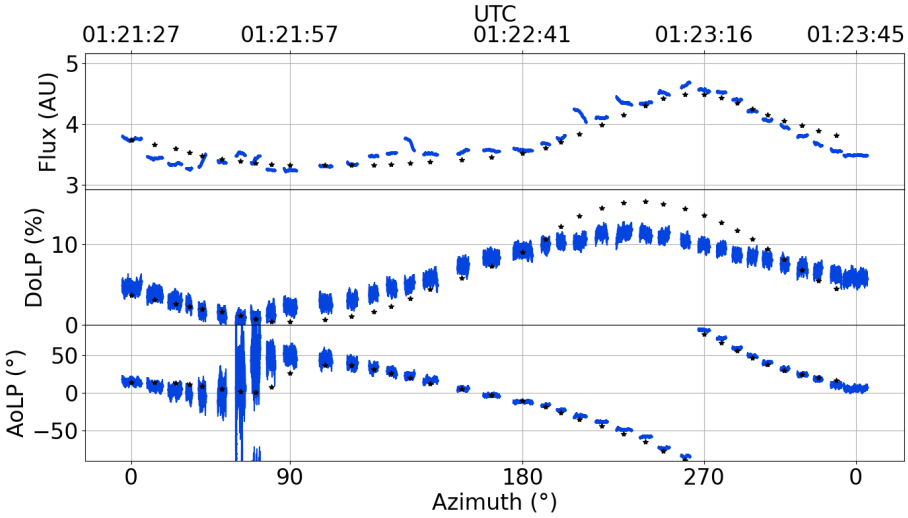

Figure 13: Same as Figure 11 for the blue line.

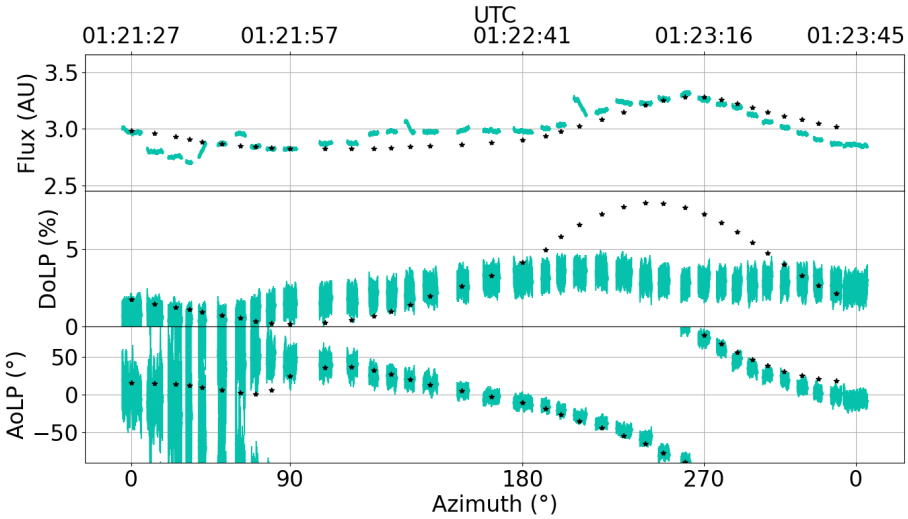

Figure 14: Same as Figure 11 for the turquoise line.

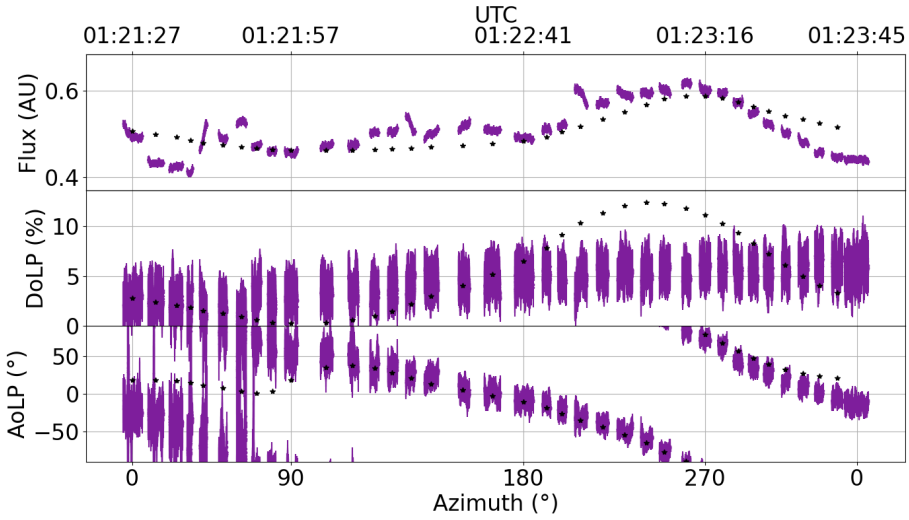

Figure 15: Same as Figure 11 for the purple line.

The results presented in this paper show the feasibility of nocturnal polarization measurements and modelisation. Our model, although currently limited to a single scattering scheme, is doomed to evolve, and constitutes a proof of concept that paves the way to further investigations of the night-sky light polarization.

Our results show that several contributions must be considered in order to explain observations: extended sources on the ground (light pollution from the nearby cities) and sources in the sky (the background) via two possible mechanisms (starlight and nightglow), plus a correction for multiple scattering. Furthermore, the atmospheric model must include Rayleigh scattering and Lorenz-Mie scattering by aerosols. We discuss below several potential applications of this model.

First, it will be used to interpret properties of the polarized lights measured at high latitudes under auroral conditions (Bosse et al., 2020), to validate or not a polarization when these are emitted in the ionosphere (Lilensten et al., 2016). The present study shows that the use of wavelengths outside the ionospheric emissions lines is crucial to determine a correct profile of aerosols, as this latter is of prime importance to understand the measured radiant flux and *DoLP*. Furthermore, in auroral conditions, ionospheric lights will strongly dominate over the integrated starlight. As a consequence, the complex picture of these emissions (2D maps) will be needed as an entry of the model. We can also imagine that in these countries where wide areas are covered with snow, the reflection of auroras on the ground might be of importance. These effects will be accounted for in an upcoming study.

In the above interpretation of mid-latitude observations, considering an unpolarized background source and the 1-low aerosol model seem compulsory to explain most of our measurements. It is difficult at this stage to reach a definitive conclusion on its origin, because we lack an absolute measure of the radiant flux. However, in the absence of any other source, we have shown that our code can also handle a polarized background source, and that its signature (if any) should be detectable despite the Rayleigh and Lorenz-Mie scattering. We have shown that a horizontally polarized uniform sky source produces *AoLP* changes along an almucantar that resemble to the ones produced by scattering within the atmosphere. It might thus be insightful to consider the possibility of the polarization by horizontal ionospheric electrical currents. These can be partially reconstructed from ground-based magnetometers (e.g. Amm & Viljanen, 1999; Pulkkinen et al., 2003). This possibility is motivated by the observation of coherent fluctuations in time

series for both the polarization parameters of auroral lights, and the electron density content in the ionosphere (Bosse et al., 2020). This may have further consequences for the study of the equatorial airglow, below the electrojet.

We have shown that the relative contribution of background lights to scattering strongly varies with the wavelength: from +43% for the longest one (orange), to +114% in the green and +219% in the shortest one (blue). Measuring how much this means in absolute units would require the knowledge of the city light spectrum (that is not provided with the input maps) as well as the instrument transfer function (such a calibration would require a dedicated study, as it depends on the photo-sensors and on the opacity of the filters used in the instrument). This higher background contribution at shorter wavelengths can be a sign that the uniform, isotropic and unpolarized background partly corrects for the effect of multiple scattering. Indeed, its contribution is expected to be higher at short wavelengths. This result is also compatible with the expected relative contributions from the city lamps, the nightglow and the starlight. On the one hand, the city contribution is likely higher in the green and orange than in the blue (i.e. the same sky emission for all three lines should lead to a relatively higher contribution for the blue). On the other hand, if we were to detect a contribution from the nightglow, we would expect relatively higher radiant fluxes in the blue and green than in the orange (which is not emitted in the ionosphere), for a constant contribution of the cities at the observation point. Thus our results are fully compatible with the nightglow emissions, showing that the method may be used for such studies. Moreover, adjusting the modeling to the observations requires a contribution from the integrated starlight (at least that for the orange). The combined contributions of the nightglow and the starlights can therefore be detected with this method even in the presence of light pollution, although we cannot distinguish yet between the two sources.

Another major result is the influence of the aerosols. The good fit between the model and the measurements at several wavelengths comes with a determination of the size distribution, profile distribution and refractive index of the aerosols. Any attempt to change drastically these parameters degrades the fit. The precise determination of the aerosol parameters is out of scope of this preliminary study. It would require for example using independent measurements (such as LIDAR) or dedicated inversion schemes in order to optimize the input model parameters. Nevertheless, we showed that the measurement of the light polarization constitutes an original way for aerosol studies at night.

Of course our model suffers from limitations, the first of which being the omission of multiple scattering. This should be implemented in future versions for a better concordance with observations. Different methods could be used to incorporate multiple scattering in POMEROL, such as forward or backward Monte Carlo approaches (Ramella-Roman et al., 2005; Yong et al., 2016), doubling adding method (Hovenier, 1971) or path integrals (Petržala, 2021). Even though this work is out of the scope of this paper, we would say that a reversed Monte-Carlo approach is particularly adapted to our model since the light sources are spread and the detector is small. This could save significant computation time but introduces difficulties for polarization tracing. We have shown that the impact of multiple scattering can be partly accounted for via the unpolarized isotropic background for the blue and longer wavelengths, without ruling out our model. Then, pollution maps are not provided for all wavelengths (but these might be calibrated with in situ measurements). Also, although we found that an isotropic sky was enough to fit our observations in the green and orange lines, a more complex model of starlight and nightglow that takes into account variations in time and space could further improve the model.

Nevertheless, our results suggest that our single-scattering polarized radiative transfer model together with our polarimeter may be used during night-time to detect light pollution even in remote areas, and to diagnose the aerosol content with for instance potential applications concerning the quality of air. The experimental technique is passive, contrary to lidars, low power consumption (less than 5 W), fully transportable in a suitcase, and can use any kind of visible source (artificial or natural such as the moon, the skylight, the airglow). These polarimeters may be deployed over a large area, thus allowing in the future a global coverage.

Acknowledgments

This work was partly funded by the French polar institute IPEV under program POLARLIS 3, number 1026. It was also funded by the Prematuration CNRS program and by the Maturation program CM180023, project PTCU Number 180018M from the SATT company Linksium. The polarimeter is patented by the CNRS and valorised by Linksium (international patent number 1873378). We thank the Programme National Soleil-Terre for its financial support. NG was partially supported by the French Centre National d'Etudes Spatiales (CNES) for the study of Earth's core dynamics in the context of the Swarm mission of ESA.

We thank Pierre Simoneau (ONERA) for useful discussions on the mesopheric nightglow.

Open research

The source code of the POMEROL model is made freely available by the authors here: `https://github.com/LeoBosse/analysis/tree/master/pomerol`.

Ground emission maps from the NOAA Earth Observations Group (Elvidge et al., 2013) are available here: `https://eogdata.mines.edu/products/vnl/`

Atmospheric profiles from the 2001 MIPAS Model Atmospheres (Remedios et al., 2007) are available here: `http://eodg.atm.ox.ac.uk/RFM/atm/`

Elevation data from the ALOS GLobal Digital Surface Model AW3D30 DSM of the Japan Aerospace Exploration Agency (Tadono et al., 2016) are available here: `https://www.eorc.jaxa.jp/ALOS/en/index_e.htm`

References

Amm, O., & Viljanen, A. (1999). Ionospheric disturbance magnetic field continuation from the ground to the ionosphere using spherical elementary current systems. *Earth, Planets and Space*, *51*(6), 431–440.

Banks, P. M., & Kockarts, G. (1973). *Aeronomy.* Springer.

Bellisario, C., Keckhut, P., Blanot, L., Hauchecorne, A., & Simoneau, P. (2014, June). O2 and OH night Airglow emissions derived from GOMOS-EnvisatInstrument. *Journal of Atmospheric and Oceanic Technology*, *31*(6), 1301-1311. doi: 10.1175/JTECH-D-13-00135.1

Bellisario, C., Simoneau, P., Keckhut, P., & Hauchecorne, A. (2020, March). Comparisons of spectrally resolved nightglow emission locally simulated with space and ground level observations. *Journal of Space Weather and Space Climate*, *10*, 21. doi: 10.1051/swsc/2020017

Bergstrom, R. W., Pilewskie, P., Schmid, B., & Russell, P. B. (2003). Estimates of the spectral aerosol single scattering albedo and aerosol radiative effects during safari 2000. *Journal of Geophysical Research: Atmospheres*, *108*(D13).

Berk, A., Conforti, P., Kennett, R., Perkins, T., Hawes, F., & Van Den Bosch, J. (2014). Modtran® 6: A major upgrade of the modtran® radiative transfer code. In *2014 6th workshop on hyperspectral image and signal processing: Evolution in remote sensing (whispers)* (pp. 1–4).

Bommier, V., Sahal-Brechot, S., Dubau, J., & Cornille, M. (2011). The theoretical impact polarisation of the O I 6300 Å red line of Earth Aurorae. , 9.

Born, M., & Wolf, E. (1999). *Principles of optics : electromagnetic theory of propagation, interference and diffraction of light*.

Bosse, L., Lilensten, J., Gillet, N., Rochat, S., Delboulbé, A., Curaba, S., ... Frédérique, A. (2020). On the nightglow polarisation for space weather exploration. *Submited to the Journal of Space Weather and Space Climate*, -.

Broadfoot, A. L., & Kendall, K. R. (1968, January). The airglow spectrum, 3100-10,000 A. *Journal of Geophysical Research*, *73*(1), 426–428. doi: 10.1029/JA073i001p00426

Bucholtz, A. (1995, May). Rayleigh-scattering calculations for the terrestrial atmosphere. *Applied Optics*, *34*(15), 2765–2773. doi: 10.1364/AO.34.002765

Burrows, J. P., Richter, A., Dehn, A., Deters, B., Himmelmann, S., Voigt, S., & Orphal, J. (1999, March). Atmospheric remote-sensing reference data from gome—2. temperature-dependent absorption cross sections of 3 in the 231–794nm range. *Journal of Quantitative Spectroscopy and Radiative Transfer*, *61*(4), 509–517. doi: 10.1016/S0022-4073(98)00037-5

Chandrasekhar, S. (1960). *Radiative Transfer*. Dover Publications Inc. Retrieved 2020-02-07, from `http://archive.org/details/RadiativeTransfer`

de Haan, J. F., Bosma, P., & Hovenier, J. (1987). The adding method for multiple scattering calculations of polarized light. *Astronomy and astrophysics*, *183*, 371–391.

Dubovik, O., Smirnov, A., Holben, B. N., King, M. D., Kaufman, Y. J., Eck, T. F., & Slutsker, I. (2000). Accuracy assessments of aerosol optical properties retrieved from Aerosol Robotic Network (AERONET) Sun and sky radiance measurements. *Journal of Geophysical Research: Atmospheres*, *105*(D8), 9791–9806. doi: 10.1029/2000JD900040

Dymond, K. F., Nicholas, A. C., Budzien, S. A., Stephan, A. W., Coker, C., Hei, M. A., & Groves, K. M. (2019, June). A Comparison of Electron Densities Derived by Tomographic Inversion of the 135.6-nm Ionospheric Nightglow Emission to Incoherent Scatter Radar Measurements. *Journal of Geophysical Research (Space Physics)*, *124*(6), 4585-4596. doi: 10.1029/2018JA026412

Elvidge, C., Baugh, K., Zhizhin, M., & Hsu, F.-C. (2013, June). Why VIIRS data are superior to DMSP for mapping nighttime lights [dataset]. *Proceedings of the Asia-Pacific Advanced Network*, *35*, 62–69. doi: 10.7125/APAN.35.7

Evans, K. F., & Stephens, G. L. (1991, January). A new polarized atmospheric radiative transfer model. *Journal of Quantitative Spectroscopy and Radiative Transfer*, *46*(5), 413-423. doi: 10022-4073/91

Finlay, C. C., Olsen, N., Kotsiaros, S., Gillet, N., & Tøffner-Clausen, L. (2016, December). Recent geomagnetic secular variation from Swarm and ground observatories as estimated in the CHAOS-6 geomagnetic field model. *Earth, Planets and Space*, *68*(1). doi: 10.1186/s40623-016-0486-1

Garcia-Saenz, A., Sanchez de Miguel, A., Espinosa, A., Crespo, A., Aragonés, N., Llorca, J., ... Kogevinas, M. (2018, April). Evaluating the association between artificial light-at-night exposure and breast and prostate cancer risk in spain (MCC-Spain study). *Environmental Health Perspectives*, *126*. doi: 10.1289/EHP1837

Grubisic, M., van Grunsven, R., Kyba, C., Manfrin, A., & Hölker, F. (2018, September). Insect declines and agroecosystems: Does light pollution matter? *Annals of Applied Biology*,

173, 180–189. doi: 10.1111/aab.12440

Hansen, J. E. (1971). Multiple scattering of polarized light in planetary atmospheres part ii. sunlight reflected by terrestrial water clouds. *Journal of Atmospheric Sciences*, *28*(8), 1400–1426.

Hansen, J. E., & Hovenier, J. W. (1971, January). The doubling method applied to multiple scattering of polarized light. *Journal of Quantitative Spectroscopy and Radiative Transfer*, *11*(6), 809-812. doi: 10.1016/0022-4073(71)90057-4

Hansen, J. E., & Travis, L. D. (1974, October). Light scattering in planetary atmospheres. *Space Science Reviews*, *16*(4), 527-610. doi: 10.1007/BF00168069

Herman, M., Balois, J. Y., Gonzalez, L., Lecomte, P., & Lenoble, J. (1986, October). Stratospheric aerosol observations from a balloon-borne polarimetric experiment. *Applied Optics*, *25*, 3573-3584. doi: 10.1364/AO.25.003573

Horvath, G., Kriska, G., Malik, P., & Robertson, B. (2009, August). Polarized light pollution: A new kind of ecological photopollution. *Frontiers in Ecology and the Environment*, *7*, 317–325. doi: 10.1890/080129

Hovenier, J. W. (1971). Multiple scattering of polarized light in planetary atmospheres. *Astronomy and Astrophysics*, *13*, 7.

Hovenier, J. W. (1971, June). Multiple Scattering of Polarized Light in Planetary Atmospheres. *Astronomy and Astrophysics*, *13*, 7.

Jaenicke, R. (1993). Chapter 1 Tropospheric Aerosols. In *International Geophysics* (Vol. 54, pp. 1–31). Elsevier. doi: 10.1016/S0074-6142(08)60210-7

King, M. D. (1986). Comparative accuracy of selected multiple scattering approximations. *Journal of Atmospheric Sciences*, *43*(8), 784–801.

Kyba, C., Kuester, T., Sanchez de Miguel, A., Baugh, K., Jechow, A., Hölker, F., ... Guanter, L. (2017, November). Artificially lit surface of Earth at night increasing in radiance and extent. *Science Advances*, *3*, e1701528. doi: 10.1126/sciadv.1701528

Kyba, C., Ruhtz, T., Fischer, J., & Hölker, F. (2011, December). Lunar skylight polarization signal polluted by urban lighting. *Journal of Geophysical Research (Atmospheres)*, *116*, 24106-. doi: 10.1029/2011JD016698

Lax, M. (1951). Multiple Scattering of Waves. , *23*(4), 287–310. Retrieved 2021-05-18, from `https://link.aps.org/doi/10.1103/RevModPhys.23.287` doi: 10.1103/RevModPhys.23.287

Leinert, C., Bowyer, S., Haikala, L. K., Hanner, M. S., Hauser, M. G., Levasseur-Regourd, A.-C., ... Witt, A. N. (1998, January). The 1997 reference of diffuse night sky brightness. *Astronomy and Astrophysics Supplement Series*, *127*(1), 1–99. doi: 10.1051/aas:1998105

Lilensten, J., Barthélemy, M., Besson, G., Lamy, H., Johnsen, M. G., & Moen, J. (2016, July). The thermospheric auroral red line Angle of Linear Polarization: Auroral angle of linear polarization. *Journal of Geophysical Research: Space Physics*, *121*(7), 7125–7134. doi: 10.1002/2016JA022941

Lilensten, J., Moen, J., Barthélemy, M., Thissen, R., Simon, C., Lorentzen, D. A., ... Sigernes, F. (2008, April). Polarization in aurorae: A new dimension for space environments studies. *Geophysical Research Letters*, *35*(8). doi: 10.1029/2007GL033006

Lorenz, L. (1890). Lysbevaegelsen i og uden for en af plane lysbolger belyst kugle". det kongelige danske videnskabernes selskabs skrifter. 6. , *6. Bind (1*, 1–62.

McFarlane, S. C. (1974, September). A Bethe theory for the polarization of impact radiation. *Journal of Physics B Atomic Molecular Physics*, *7*(13), 1756-1771. doi: 10.1088/0022-3700/7/13/021

Mie, G. (1908). Beiträge zur Optik trüber Medien, speziell kolloidaler Metallösungen. *Annalen der Physik*, *330*(3), 377–445. doi: 10.1002/andp.19083300302

Miller, S. D., Straka, W., Mills, S. P., Elvidge, C. D., Lee, T. F., Solbrig, J., ... Weiss, S. C. (2013, December). Illuminating the Capabilities of the Suomi National Polar-Orbiting Partnership (NPP) Visible Infrared Imaging Radiometer Suite (VIIRS) Day/Night Band. *Remote Sensing*, *5*(12), 6717–6766. doi: 10.3390/rs5126717

Mills, S., Weiss, S., & Liang, C. (2013, September). VIIRS day/night band (DNB) stray light characterization and correction. In J. J. Butler, X. J. Xiong, & X. Gu (Eds.), *SPIE Optical Engineering + Applications* (p. 88661P). San Diego, California, United States. doi: 10.1117/12.2023107

Mishchenko, M. I., Travis, L. D., & Lacis, A. A. (2002). *Scattering, absorption, and emission of light by small particles*. Cambridge University Press.

Ougolnikov, O. S., & Maslov, I. A. (2002, May). Multicolor Polarimetry of the Twilight Sky: The Role of Multiple Light Scattering as a Function of Wavelength. *Cosmic Research*, *40*(3), 224-232.

Parihar, N., Radicella, S. M., Nava, B., Migoya-Orue, Y. O., Tiwari, P., & Singh, R. (2018, May). An investigation of the ionospheric F region near the EIA crest in India using OI 777.4 and 630.0 nm nightglow observations. *Annales Geophysicae*, *36*(3), 809-823. doi: 10.5194/angeo-36-809-2018

Petržala, J. (2021, April). Revision of path-integral approach to radiative transfer. *Journal of Quantitative Spectroscopy and Radiative Transfer*, 107670. doi: 10.1016/j.jqsrt.2021.107670

Plane, J., Oetjen, H., de Miranda, M., Saiz-Lopez, A., Gausa, M., & Williams, B. (2012, January). On the sodium D line emission in the terrestrial nightglow. *Journal of Atmospheric and Solar-Terrestrial Physics*, *74*, 181–188. doi: 10.1016/j.jastp.2011.10.019

Pulkkinen, A., Amm, O., & Viljanen, A. (2003). Ionospheric equivalent current distributions determined with the method of spherical elementary current systems. *Journal of Geophysical Research: Space Physics*, *108*(A2).

Pust, N. J., & Shaw, J. A. (2011). Comparison of skylight polarization measurements and MODTRAN-P calculations. *Journal of Applied Remote Sensing*, *5*, 18.

Ramella-Roman, J. C., Prahl, S. A., & Jacques, S. L. (2005). Three monte carlo programs of polarized light transport into scattering media: part i. *Optics Express*, *13*(12), 4420–4438.

Rayleigh, J. W. S. B. (1871). On the scattering of light by small particles. *The London, Edinburgh, and Dublin Philosophical Magazine and Journal of Science*, *41*, 447—454. doi: 10.1080/14786447108640507

Remedios, J., Leigh, R., Waterfall, A., Moore, D., Sembhi, H., Parkes, I., ... Hauglustaine, D. (2007). Mipas reference atmospheres and comparisons to v4. 61/v4. 62 mipas level 2 geophysical data sets [dataset]. *Atmospheric Chemistry and Physics Discussions*, *7*(4), 9973–10017.

Santer, R., Herman, M., Tanre, D., & Lenoble, J. (1988, November). Characterization of stratospheric aerosol from polarization measurements. *Journal of Geophysical Research: Atmospheres*, *93*(D11), 14,209-14,221. doi: 10.1029/JD093iD11p14209

Staude, H. (1975). Scattering in the earth's atmosphere: Calculations for milky way and zodiacal light as extended sources. *Astronomy and Astrophysics*, *39*, 325.

Tadono, T., Nagai, H., Ishida, H., Oda, F., Naito, S., Minakawa, K., & Iwamoto, H. (2016, June). *Generation of the 30 m-mesh global digital surface model by alos prism [dataset]* (Vol. XLI-B4). https://doaj.org. Copernicus Publications. doi: 10.5194/isprs-archives-XLI-B4-157-2016

Tashchilin, A., & Leonovich, L. (2016, September). Modeling nightglow in atomic oxygen red and green lines under moderate disturbed geomagnetic conditions at midlatitudes. *Solar-Terrestrial Physics*, *2*(4), 94-106. doi: 10.12737/21491

Ugolnikov, O. S., Postylyakov, O. V., & Maslov, I. A. (2004, September). Effects of multiple scattering and atmospheric aerosol on the polarization of the twilight sky. *Journal of Quantitative Spectroscopy Radiative Transfer*, *88*, 233-241. doi: 10.1016/j.jqsrt.2003.12.033

van de Hulst, H. C. (1981). *Light scattering by small particles*. New York: Dover Publications.

Vargas, F. (2019, November). Traveling Ionosphere Disturbance Signatures on Ground-Based Observations of the O(^{1}D) Nightglow Inferred From 1-D Modeling. *Journal of Geophysical Research (Space Physics)*, *124*(11), 9348-9363. doi: 10.1029/2019JA027356

Yong, H., Guo-Dong, S., & Ke-Yong, Z. (2016, March). Backward and forward monte carlo method in polarized radiative transfer. *The Astrophysical Journal*, *820*(1), 9. doi: 10.3847/0004-637X/820/1/9

Zielinska-Dabkowska, K. (2018, January). Make lighting healthier. *Nature*, *553*. doi: 10.1038/d41586-018-00568-7

Ångström, A. (1929). On the atmospheric transmission of sun radiation and on dust in the air. *Geografiska Annaler*, *11*, 156–166. doi: https://doi.org/10.2307/519399

Appendix A Computation of the radiant flux measured by our virtual instrument

A1 Computation of the radiant flux measured by the virtual instrument

In this appendix, we compute the radiant flux measured by a virtual instrument in A when the light is emitted by a single point source E, and scattered at a single point R along the line of sight (see Figure 2). We describe each intermediate step in order for the reader to understand and reproduce our results.

We use here the units used by POMEROL, with the scale factor implemented in the code. The scale factor has no effect on the dimensional analysis, but are kept here for more transparency on the code.

First, the source is fully described by its radiance L_E in nW/m^2/sr as given by the input map (see section 3.1), and its surface area A_E in m^2. It is considered small enough to be approximated as a point source of radiant intensity $I_E = L_E A_E$ in nW/sr. Its emission is considered isotropic. From this, the irradiance E_E reaching the scattering volume in R is (in nW/m^2):

$$E_E = L_E \Omega_E \exp(-\tau_{ER}) \tag{A1}$$

$$= L_E \frac{A_E}{d_{ER}^2} \exp(-\tau_{ER}) \tag{A2}$$

where $\Omega_E = A_E/d_{ER}^2$ is the solid angle of the emission surface as seen from the scattering point at a distance d_{ER} (in m), and τ_{ER} is the effective optical depth of the atmosphere between the emission in E and the scattering volume Γ in R (see equations A21 to A24).

The radiant intensity I_R (in nW/sr) scattered by the volume of atmosphere Γ around R is:

$$I_R = E_E \, \sigma \, \frac{\Phi(\theta)}{4\pi} \tag{A3}$$

where σ (in m^2) is the total scattering cross-section of the molecules or particles, θ is the scattering angle and $\Phi(\theta)$ is the scattering phase function (see equation A5 and following text). By definition the phase function Φ is dimensionless and normalized across a sphere (e.g. Mishchenko et al. (2002); Chandrasekhar, S. (1960)), such that:

$$1 = \frac{1}{2} \int_{\theta=0}^{\pi} \Phi(\theta) \, \sin(\theta) d\theta \tag{A4}$$

It ensues that $\Phi(\theta)/(4\pi)$ has units of sr^{-1}. The phase function Φ and total scattering cross-section σ to consider is different whether we consider Rayleigh scattering on air molecules or Lorenz-Mie scattering on aerosols.

$$\Phi_{ray}(\theta) = \frac{3}{4} \left(1 + \cos^2 \theta\right) \tag{A5}$$

is the Rayleigh phase function (Bucholtz, 1995). It does not take into account molecular anisotropy effects. This approximation does not affect our results significantly, but could be improved in the future if necessary using a formula from Chandrasekhar (Chandrasekhar, S., 1960). The aerosol phase function $\Phi_{aer}(\theta)$ is computed using Lorenz-Mie scattering theory (Lorenz, 1890; Mie, 1908; Born & Wolf, 1999) and depends on the aerosol model parameters listed in Table 1. For the air molecules, the scattering cross-section is

$$\sigma_{ray} = \beta \, \Gamma \tag{A6}$$

and for the aerosols, it is:

$$\sigma_{aer} = \bar{\omega} C_{ext} \Gamma \tag{A7}$$

with β the Rayleigh scattering coefficient in m^{-1} as described in Bucholtz (1995) (see equations A18 to A20), $\bar{\omega}$ the single scattering albedo of the aerosol, C_{ext} the extinction coefficient of the aerosol in m^{-1} and Γ the scattering volume centered around R in m^3. Γ, the scattering volume

Coefficient	$0.2 < \lambda\,(\mu m) < 0.5$	$0.5 < \lambda\,(\mu m)$
A_{ray}	7.68246×10^{-4}	10.21675×10^{-4}
A_{op}	6.49997×10^{-3}	8.64145×10^{-3}
B	3.55212	3.99668
C	1.35579	0.00110298
D	0.11563	0.0271393

Table A1: Parameters used in equation (A20). (Bucholtz, 1995)

(see Fig. 2), is a truncated cone defined by ε the half aperture angle of the virtual instrument (similar to that of the real polarimeter), d_{AR} and l the height of the cone. It is given by

$$\Gamma = \frac{\pi}{3}\tan^2(\varepsilon)\; l\; \left(3d_{AR}^2 + l^2/4\right)\; . \tag{A8}$$

Finally, the radiant flux in nW measured by the virtual instrument in A is:

$$F_A = I_R \Omega_A \exp(-\tau_{AR}) \tag{A9}$$

$$= \frac{I_R \Sigma}{d_{AR}^2}\exp(-\tau_{AR}) \tag{A10}$$

Where Ω_A is the solid angle (in sr) of the detector as seen from the scattering volume in R, Σ is the surface area of the detector (in m^2), d_{AR} is the distance from the scattering point to the detector (in m) and τ_{AR} is the effective optical depth along the path from R to A. Developing I_R into the initial parameters gives us:

$$F_A = I_R \frac{\Sigma}{d_{AR}^2}\exp(-\tau_{AR}) \tag{A11}$$

$$= E_E \sigma \frac{\Phi(\theta)}{4\pi}\frac{\Sigma}{d_{AR}^2}\exp(-\tau_{AR}) \tag{A12}$$

$$= L_E \frac{A_E}{d_{ER}^2}\exp(-\tau_{ER}-\tau_{AR})\sigma\frac{\Phi(\theta)}{4\pi}\frac{\Sigma}{d_{AR}^2} \tag{A13}$$

$$= \frac{L_E}{4\pi}\frac{A_E}{d_{ER}^2}\frac{\Sigma}{d_{AR}^2}\exp(-\tau_{ER}-\tau_{AR})\sigma\Phi(\theta) \tag{A14}$$

At this point, we replace the scattering coefficient by the corresponding expression, whether we consider the Rayleigh scattering on air molecules, or the Mie scattering on aerosols. This gives:

$$F_A^{ray} = \frac{L_E}{4\pi}\frac{A_E}{d_{ER}^2}\frac{\Sigma}{d_{AR}^2}\exp(-\tau_{ER}-\tau_{AR})\Gamma\beta\Phi_{ray}(\theta) \tag{A15}$$

and:

$$F_A^{aer} = \frac{L_E}{4\pi}\frac{A_E}{d_{ER}^2}\frac{\Sigma}{d_{AR}^2}\exp(-\tau_{ER}-\tau_{AR})\Gamma\bar{\omega}C_{ext}\Phi_{aer}(\theta) \tag{A16}$$

The total radiant flux measured by our virtual instrument is then the sum of both contributions as:

$$F_A = \frac{L_E}{4\pi}\frac{A_E}{d_{ER}^2}\frac{\Sigma}{d_{AR}^2}\,\Gamma\,\exp(-\tau_{ER}-\tau_{AR})\left[\beta\Phi_{ray}(\theta) + \bar{\omega}C_{ext}\Phi_{aer}(\theta)\right] \tag{A17}$$

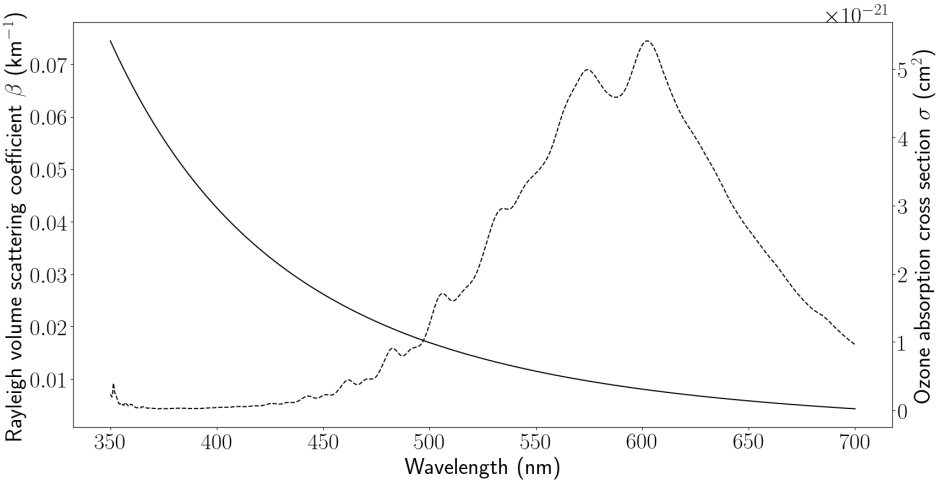

Figure A1: Rayleigh scattering coefficient at sea level $\beta_0(\lambda) = \beta(\lambda, z)_{|z=0}$ (full line, left, see equation A19), and ozone absorption cross section $\sigma_{O_3}(\lambda)$ (dashed line, right), as a function of wavelength.

We describe below in more detail the computations of all the physical quantities used to compute F_A. Classically, the Rayleigh scattering cross section per molecule is (Rayleigh, 1871; Mie, 1908; Bucholtz, 1995):

$$C^{ray} = \frac{24\pi^3}{\lambda^4 N_s^2} \left(\frac{m_s^2 - 1}{m_s^2 + 2} \right)^2 \frac{6 + 3\rho_n}{6 - 7\rho_n}, \tag{A18}$$

with λ the wavelength, N_s the molecular number density for standard air, m_s the refractive index of standard air at λ and ρ_n the depolarization factor. In our model, this is accounted for via the Rayleigh scattering coefficient $\beta(\lambda, z)$ (in m^{-1}). Following Bucholtz (1995), it is approximated as

$$\beta(\lambda, z) = \beta_0(\lambda) \frac{P(z)}{P_0} \frac{T_0}{T(z)}, \tag{A19}$$

with $P(z)$ and $T(z)$ the atmospheric pressure and temperature profiles. $P_0 = 101\,325$ Pa and $T_0 = 288.15$ K are the pressure and temperature at sea level, and

$$\beta_0(\lambda) = A_{ray} \lambda^{-(B + C\lambda + D/\lambda)}, \tag{A20}$$

with λ the wavelength (in μm). This approximation takes into account the depolarization (or King) factor. Values for coefficients A_{ray}, B, C and D are given in Table A1, and $\beta(\lambda, z)_{|z=0}$ is shown in Figure A1.

The effective optical depth τ of the atmosphere between E and R (and similarly between R and A), is the sum of three contributions from Rayleigh scattering, ozone absorption and aerosol extinction:

$$\tau = \tau_{ray} + \tau_{O_3} + \tau_{aer}. \tag{A21}$$

The optical depth from Rayleigh scattering between E and R at respective altitudes z_E and z_R is (Bucholtz, 1995):

$$\tau_{ray}(z_E, z_R, \lambda) = \tau_0(\lambda) \frac{|P(z_E) - P(z_R)|}{P_0}, \tag{A22}$$

where $\tau_0(\lambda)$ follows equation (A20) with A_{ray} replaced by A_{op} (value given in Table A1). The optical depth for ozone absorption is

$$\tau_{O_3}(z_E, z_R, \lambda) = \sigma_{O_3}(\lambda) \int_{z_E}^{z_R} N_{O_3}(z')dz' \,, \tag{A23}$$

where $N_{O_3}(z)$ is the ozone number density at altitude z (provided with the atmospheric profile, see Figure 1) and $\sigma_{O_3}(\lambda)$ (shown in Figure A1) is the ozone absorption cross section at wavelength λ and a fixed temperature of 273 K (Burrows et al., 1999). This is an approximation which could be refined in future versions with a dependence on temperature. The optical depth for aerosols is

$$\tau_{aer}(z_E, z_R, \lambda) = \int_{z_E}^{z_R} C_{ext}^{aer}(z', \lambda)dz' \,. \tag{A24}$$

A2 Computation of the polarization parameters of the light reaching the virtual instrument

To compute the *DoLP* and *AoLP* of the light reaching the virtual instrument, one must use the Stokes parameters I, Q and U. In the case of light coming from a single point source and scattered at a single point along the line of sight, the polarization is defined with respect to the scattering plane containing the incoming and scattered rays. In this case, the polarization induced by Rayleigh and Mie scattering can only be either perpendicular or parallel to the scattering plane. So we assume $U = 0$. For example, the *DoLP* of a light beam scattered at an angle θ via Rayleigh scattering is (McFarlane, 1974)

$$DoLP^{ray}(\theta) = |Q^{ray}(\theta)| = \frac{\sin^2\theta}{1 + \cos^2\theta} \,. \tag{A25}$$

and is always perpendicular to the scattering plane (which means that $AoLP = 0°$, $Q > 0$ and $U = 0$). We use the Lorentz-Mie scattering theory to compute the polarization induced by aerosol scattering. Here, we have the three Stokes parameters coding for linear polarization defined with respect to the scattering plane: I_s (computed in the previous section), Q_s computed from Rayleigh and Lorenz-Mie scattering theory and $U_s = 0$. These translate to a radiant flux (see previous section), a $DoLP_s = |Q_s|$ and an $AoLP_s = 0$ or 90 degrees depending on the sign of Q_s.

However, note that the orientation of the scattering plane is different for each point source in the input emission map. Therefore, it is not possible to add the Stokes parameters of each single contribution directly. Before, we must harmonize the definition of the polarization so that each single contribution is defined with respect to the same orientation. For this, we use a reference frame attached to the instrument defined as $\mathcal{R}_* = (\mathbf{x}_*, \mathbf{y}_*, \mathbf{z}_*)$ such that $\mathbf{x}_*$ points along the line of sight and $\mathbf{y}_*$ is horizontal in the plane of the detector. With this, we can express the normal vector of the instrument's plane of reference as $n = (0, 0, 1)$. This orientation is chosen so that, when the instrument points horizontally, $AoLP = 0°$ for a vertical polarization and $AoLP = 90°$ for a horizontal polarization. The scattering plane normal vector can be expressed as $(0, y_s, z_s)$ in this reference frame. All necessary derivations of y_s and z_s from the instrument pointing direction and the light source relative position are detailed by Bosse et al. (2020) in their appendix C. We define the *AoLP* measured by the instrument as $0.5 \arctan(y_s/z_s)$ in the case where $Q_s > 0$ (or $0.5 \arctan(z_s/y_s)$ for $Q_s < 0$). The *AoLP* is positive in the trigonometric direction (anticlockwise) when looking towards the source. The *AoLP* is π periodic, such that we define it in the interval $[-90°, 90°]$. The transformation of the Stokes parameters from one reference plane to the other correspond to a rotation of the scattering plane to align to the instrument plane of reference. The 2D rotation matrix for an angle α is expressed as

$$R(\alpha) = \begin{pmatrix} \cos\alpha & \sin\alpha \\ -\sin\alpha & \cos\alpha \end{pmatrix} . \tag{A26}$$

So the Stokes parameters in the reference plane of the instrument can be computed as:

$$\begin{pmatrix} Q \\ U \end{pmatrix} = R(2\,AoLP) \begin{pmatrix} Q_s \\ U_s \end{pmatrix} . \tag{A27}$$

Only when the Stokes parameters for each single contribution have been rotated to match the global reference frame, one can sum the Stokes parameters to obtain the total polarization measured by the virtual instrument, such as described in the main article in equation 8. We finally can use 5 to convert the Stokes parameters to the *DoLP* and *AoLP* notation.